論文 / 著書情報
Article / Book Information

題目(和文)	ショウジョウバエにおける頑強な動き検知を実現する神経機構の解明
Title(English)	Studies on Neural Basis of Robust Motion Perception in Drosophila melanogaster
著者(和文)	鈴木力憲
Author(English)	Yoshinori Suzuki
出典(和文)	学位:博士（理学）, 学位授与機関:東京工業大学, 報告番号:甲第9930号, 授与年月日:2015年6月30日, 学位の種別:課程博士, 審査員:青西　亨,樺島　祥介,山村　雅幸,中村　清彦,木賀　大介
Citation(English)	Degree:, Conferring organization: Tokyo Institute of Technology, Report number:甲第9930号, Conferred date:2015/6/30, Degree Type:Course doctor, Examiner:,,,,
学位種別(和文)	博士論文
Type(English)	Doctoral Thesis

学位論文

Studies on Neural Basis of Robust Motion Perception in *Drosophila melanogaster*

ショウジョウバエにおける頑強な動き検知を実現する神経機構の解明

Yoshinori Suzuki

鈴木力憲

Contents

Abstract 4

1 Introduction 5

1-1 General Introduction 5

1-2 Application to robotics 8

1-3 Goal and Methodology 9

2 Robust recognition of wide-field motion direction and its underlying neural mechanisms 12

Yohinori Suzuki, Hideaki Ikeda, Takuya Miyamoto, Hiroyoshi Miyakawa, Toru Aonishi and Takako Morimoto, Noise-robust recognition of wide-field motion direction and the underlying neural mechanisms in *Drosophila melanogaster*, Scientific Reports, 5, 10253 (2015) doi: 10.1038/srep10253

2-1 Fly optomotor response 12

2-2 Materials and Methods 15

2-2-1 Flies 15

2-2-2 Visual Display and Stimuli 15

2-2-3 Behavioral experiments 16

2-2-4 Whole-cell patch clamp recordings 17

2-2-5 Immunohistochemistry 19

2-2-6 Computer simulations 20

2-2-7 Data analysis 25

2-3 Results 27

2-3-1 Robust perception of wide-field motion with strong noise 27

2-3-2 HS cell activities 29

2-3-3 Effects of binocular vision 32

2-3-4 Neural algorithms underling robust motion perception 33

2-4 Conclusions and Discussion 36

3 Effects of binocular integration on ego-motion estimation 45

Yohinori Suzuki, Takako Morimoto, Hiroyoshi Miyakawa and Toru Aonishi, Cooperative integration and representation underlying bilateral network of fly motion-sensitive neurons, PLoS ONE, (2014)

doi:10.1371/journal.pone.0085790

3-1 Ego-motion 45
3-2 Wide-field motion sensitive neurons 46
3-3 Bilateral network of wide-field motion sensitive neurons 48
3-4 Materials and Methods 52
3-4-1 Fly visual system 52
3-4-2 Bilateral horizontal LPTCs network 53
3-4-3 Conductance-based model (Detailed model) 54
3-4-4 Mimicking visual stimuli 56
3-4-5 Connection properties 59
3-4-6 Formal neuron model (Reduced model) 61
3-4-7 Data analysis 64
3-5 Results 66
3-5-1 Modification of H2 cell by contralateral LPTC activities 66
3-5-2 Enhancement of synchronization between spiking LPTCs in the in-phase motion 69
3-5-3 Synchronous activities of the bilateral network represent binocular stimuli 71
3-5-4 Effect of interhemispheric electrical couplings on population coding in the bilateral network 75
3-5-5 Properties of population coding in the reduced model 77
3-6 Conclusions and Discussion 79
3-6-1 Summary of results and conclusion 79
3-6-2 Intuitive explanation of the binocular motion integration 80
3-6-3 Reliability of modeling with the ML model 82
3-6-4 Potential of synchronized coding of binocular motion in spiking LPTCs other than H2 cells 84
3-6-5 Significance of sensitive response to in-phase motion in OMR 86
3-6-6 Importance of our analysis method 87
4 Summary 90
References 93

Figures 103

Tables 137

Abstract

To address a neural basis of robust behavioral control in the natural environment, I focused on the motion perception in *Drosophila melanogaster*. First, to reveal how the fly brain processes a noisy wide-field motion stimulus and guarantees robust reactions, I measured and compared the optomotor response and the activity of motion sensitive neurons. Second, to reveal how ego-motion is encoded by the bilateral network of the neurons, I constructed an accurate model of the neural network and simulated its activity. From these two studies I found that the robust motion perception emerges from an early stage of visual system prior to the bilateral network and the network more efficiently encodes a rotational ego-motion than translational one by binocular integration.

1 Introduction

1-1 General Introduction

The brain controls behavior and is involved in mind, cognition and emotion. To uncover a central enigma of the brain function, how does the brain work to accomplish such difficult tasks, has been attracting interest from many people not just scientists. However, it is not so easy to reveal the human brain function because of the complexity of the brain that is constructed by the estimated 100 billion neurons. To uncover the function of the brain, we also need to directly measure the activity of neurons *in vivo*. Since Hodgkin and Huxley measured action potentials from a squid giant axon in 1939 (Hodgkin and Huxley, 1939), several methods of measuring the activity of neuron or neurons have been developed. Examples are patch clamp or intracellular recording and Ca^{2+} imaging technic which allow us to measure the membrane potential of single neuron and the intracellular concentration of Ca^{2+} around a large numbers of neurons, respectively. However, of course, it is hard to observe the activities of human brain by

such techniques, and there is an ethical problem also here.

In such situation, various animals except for human, such as monkey, mouse, zebrafish, *Caenorhabditis elegans* and *Drosophila melanogaster*, have been used as model animals for neuroscience. Among these animals, *Drosophila melanogaster* (*D.melanogaster* or fruit fly) is one of the especially successful animal in neuroscience. Fruit fly is a tiny insect that is about 5 mm in body length and has two major nerve tissues that are the brain involved in sensory information processing and ventral nerve code (VNC). The fly brain is constructed by the approximately 10 million neurons and the size is approximately 600 μm. In spite of tiny size of the brain, there is remarkable diversity in their behavior. For example, they have an ability to do associative learning between odor (de Belle and Heisenberg, 1994; Waddell and Quinn, 2001), color (Vogt et al., 2014), space (Neuser et al., 2008; Ofstad et al., 2011), visual features (Liu et al., 2006) and an attractive or aversive stimulus, to mate with complicated courtship song, and to also do same decision making tasks (Tang, 2001; van Swinderen, 2007; van

Swinderen and Flores, 2007; van Swinderen et al., 2009; Zhang et al., 2007).

The greatest cause of fruit fly's success as model system is a large variety of molecular and genetic tools available to visualize and manipulate neurons. Although it is also possible to use same genetic tools in mice or other model animals, we can easily introduce powerful genetic tools in fruit fly than the other animals because of simplicity breeding, its short lifespan and brief interbreeding. One of the most useful genetic tool in *Drosophila* is GAL4/UAS system (Brand and Perrimon, 1993). This system enables us to express an arbitrary protein in an arbitrary part of brain. And, we can also genetically manipulate a 'single' neuron by combining such genetic tools. By this system, we can visualize specific neurons and manipulate its membrane properties such as channel expression pattern. For example, we are able to clarify a causal relationship between specific behavior and neural activities exceed a correlation by expressing a heat or light activated ion-channel to manipulate membrane potentials. It is called 'optogenetics', and it became a powerful tool for neuroscience.

1-2 Application to robotics

Recently, the concern with applying knowledge from the insect brain research to robotics has been growing. Although the insect brain so much smaller than any microcomputer we know, it has amazingly high ability to process information and use a lot less energy. If we can develop 'artificial insect brain', it makes a substantial contribution for human society. In this trend, scientists of University of Sheffield and Sussex launched a project called 'Green Brain' (see references "Green Brain Project"). This project aim to create a robot that thinks, sense, and acts like a honeybee by combining computational modeling, learning and decision theory, computing methods, and robotics with data from neurobiological experiments in *Apis mellifera*. Another similar project called 'Robobees' also started up in Harvard University (see references "Robobees"). And furthermore, recently, a several number of studies have been conducted on applying neural algorithms of visual processing in fruit fly to controlling an autonomous

flight robot ‘drone’ (Beyeler et al., 2009; Moeckel and Liu, 2007; 2010; Reichel et al., 2005). Autonomous flight is one of the most attractive technique in a broad range of fields, such as disaster rescue robot and space plane. To automatically control the drone appropriately and robustly, in general, visual images from cameras have to be processed at ultra high speed. In fruit fly, they can processed visual image from compound eyes and control there posture by impossible speed at any our visual processing algorithm (Muijres et al., 2014; Reyn et al., 2014). Therefore, uncovering how does the fly brain such fast and robustly process visual information may contribute to the development of robot control, and its demand rises.

1-3 Goal and Methodology

As mentioned above, the fly brain has ability to fast and robustly process information from the outside world. However, as a matter of course, not only fly but also any other animals have this amazing ability. Because sensory stimuli often became noisy in nature, animals have to response

appropriately and robustly even to such unapparent stimuli. Therefore, this issue is one of most important problem in neuroscience, how the brain processes unapparent information and guarantees robust behavioral reactions. Answering these questions will provide a better understanding of the neural mechanisms controlling behavior in natural environments, and may also contribute to the development of robust robot control.

The goal of this study is to uncover the neural mechanisms underling robust information processing. In this study, I focused on the 'ego-motion' perception in visual system of *Drosophila melanogaster* as a model system. 'Ego-motion' is defined as the motion around their body axis within an environment. The details are to be mentioned later (see section 3-1). In most sight reliant animals not just fly, ego-motion is estimated by visual images from eyes, and it plays dominant role in their motion control. There are two major neuroscientific problems or difficulties from receiving visual information to ego-motion estimation. First, the perception of the wide-field motion direction in a receptive field of each eye. Second, the

estimation of ego-motion by integrating the wide-field motion information from the two eyes.

In this study, I have a question and an objective for each problem mentioned above. First, how is the wide-field motion direction robustly perceived in the fly visual system? To reveal this question, I measured and compared the optomotor response and the activity of motion sensitive neurons to unapparent motion stimuli (section 2). Second, how dose the bilateral network of the neurons integrate the motion information from respective eyes? To unclear this question, I constructed an accurate model of the neural network and simulated its activity (section 3).

2 Robust recognition of wide-field motion direction and its underlying neural mechanisms

2-1 Fly optomotor response

The optomotor response (OMR) is an important behavioral reaction to a sensory stimulus; it is observed in most sight-reliant animals, from vertebrates to invertebrates. The OMR is a compensatory reaction to wide-field motion or ego-motion to stabilize a retinal image and is crucial for course control during flight (Fry et al., 2009; Kirchner and Srinivasan, 1989; Srinivasan et al., 1996), walking (Seelig et al., 2010; van Swinderen and Flores, 2007), swimming (Jones, 1963), and also escaping (Fotowat et al., 2009). A considerable number of studies have been conducted on the neural and computational mechanisms underlying the OMR in the blowfly visual system (Egelhaaf and Borst, 1993), and more recently in *Drosophila melanogaster* (Joesch et al., 2008). Both systems possess almost the same neural structures and functions (Borst et al., 2010). Retinotopically processed motion information converges in a set of wide-field motion-sensitive neurons called lobula plate tangential cells (LPTCs) (Borst

and Euler, 2011; Borst et al., 2010). LPTCs involve three horizontal system (HS) cells that respond to horizontal wide-field motion stimuli (Hausen, 1982; Joesch et al., 2008). During preferred direction (PD) motion stimulation, HS cell membrane potentials are depolarized, whereas they are hyperpolarized during antipreferred or null direction (ND). Previous studies have shown that HS cells activation induces head yaw, flight, and walking OMR (Blondeau, 1981; Haikala et al., 2013; Heisenberg et al., 1978), suggesting a strong association between HS cell activity and the OMR. Response properties of either HS cells or the OMR to several stimulus features such as speed, contrast, and pattern of motion stimulus have been thoroughly investigated. However, few studies have simultaneously investigated both the OMR and HS cell activity in response to motion stimuli with motion noise, and the relationship between the OMR and HS activity in this context remains poorly understood.

Here, we studied the properties of the OMR to wide-field motion stimuli with random dot noise and compared it with the neural activity of HS

cells. Our results obtained with signal classification theory, receiver operating characteristic (ROC) analysis, revealed that flies robustly perceive wide-field motion direction even in the stimulus contains a considerable amount of noise, and HS cell activity accounts for this noise-robustness. Direct comparisons between behavior and neural activity by ROC analysis could reveal the quantitative correspondence of robust performance under the noisy condition. Furthermore, we performed simulation studies to examine the possible neural mechanisms underlying this feature of HS activity. This study provides a physiological basis for robust perception of wide-field motion stimuli with noise.

2-2 Materials and Methods

2-2-1 Flies

Fly stocks were reared on conventional medium that included cornmeal (Oriental Yeast Inc., Tokyo, Japan), yeast (Asahi Food and Health Care, Tokyo, Japan), and agar (Ina, Nagano, Japan) at 24°C under a 12:12-h light/dark schedule. Female adult flies 1–4 days after eclosion were selected for use in all experiments. I used wild-type Canton-S for behavioral experiments and UAS-GCamp3; R27B03-Gal4 (a generous gift from Dr. Vivek Jayaraman) for electrophysiological studies to label all HS cells.

2-2-2 Visual Display and Stimuli

I used a LED insect arena system (Metrix Technology Corp., New York, NY, USA (Reiser and Dickinson, 2008)). The system consists of a green LED display spanning 360° in azimuth ±60° (96 × 16 pixels) for behavioral experiments and spanning 300° in azimuth and ±60° (80 × 16 pixels) for electrophysiological studies to present flies with horizontally moving stripe

patterns. These patterns were moved by turning the LED light on and off, therefore, they did not move continuously. Because of this, spike-like changes in membrane potentials were often elicited (Schnell et al., 2014). To build motion stimuli with noise, we superimposed a random dot pattern independent from frame to frame on CW- and CCW-moving vertically striped square-wave gratings (8 pixels, approximately 30° per cycle). I modified a specific intensity of random dots (R_I: 0.2, 0.4, 0.6, 0.8, 1.0) to control an SNR of visual motion. In each frame, an LED is selected at the probability of 0.4 and turned on as a random dot. If the "random dot" LED is placed on the bright bar in the original stripe pattern, the intensity of random dot (R_I) is subtracted from the bright bar. Thus, the total luminance of the LED display is kept constant. I defined SNR for motion stimulus as

$$SNR = 10 \log_{10} \frac{1 + 0.4R_I}{0.4R_I}$$

2-2-3 Behavioral experiments

I measured the head yaw angle as an indicator of the OMR as

described previously (Kikuchi et al., 2013). Briefly, cold-anesthetized flies were tethered at the thorax to a steel pin with glue. To minimize body movement without affecting head movement, the legs were stuck together with nail polish. The fly was placed in the center of LED arena. Head movements were recorded with a CCD camera (Hamamatsu Photonics Inc., Hamamatsu, Japan). Images were collected at a frame rate of 25 or 30 Hz. After video recording, we used tracing software (PTV, Digimo, Japan) to measure the head yaw angle around the dorsoventral axis as the OMR. The stripe pattern was turning for 10 s each in CW and CCW directions. The optimal frequency to elicit an Drosophila OMR is around 4 Hz (Duistermars et al., 2007; Kikuchi et al., 2013; Schnell et al., 2014). In this study, we used 1 and 4 Hz. The intervals for each trial were not less than 5 s.

2-2-4 Whole-cell patch clamp recordings

Preparation of flies and recording protocols were modified a previously published protocol (Maimon et al., 2010). Briefly, flies were

cold-anesthetized and attached to a hole in the center of Palafilm sheet with the head bent down using two component silicon glues (KWIK-SIL, WPI, Sarasota, FL, USA). To reduce the stress caused by the restraint, I did not clip all six legs or glue the proboscis to the head. After attaching to the holder, a portion of cuticle was removed in saline (130 mM NaCl, 5 mM KCl, 2 mM $MgCl_2[6H_2O]$, 2 mM $CaCl_2[2H_2O]$, 36 mM saccharose, and 5 mM HEPES [pH 7.3]). To remove the rest of the covering tissue, collagenase (0.5 mg/ml, Yakult, Tokyo, Japan) dissolved in extracellular saline was added locally just above the HS cell somata with a micropipette using positive pressure for approximately 30 s. I performed whole-cell patch-clamp recordings on HS cells in the right brain hemisphere. The membrane potential was recorded by the patch-clamp amplifier (Axopatch 1D, Axon Instruments, Foster City, CA, USA). The recording electrode had 7–12 MΩ resistance, and the sampling frequency was 10 kHz. HS cells were observed using a 40× water-immersion objective (RAMPlan FL N; Olympus, Tokyo, Japan), a microscope (BX51WI, Olympus). Patch-clamp electrodes contained

an intracellular solution comprised of 140 mM K-aspartate, 10 mM HEPES, 1 mM KCl, 4 mM MgATP, 1 mM EGTA, and 0.5 mM NaGTP (pH 7.3). In the experiment shown in Figure 3B, the intracellular solution included 6 mM biocytin-hydrazide to visualize the HS cell's morphology. Because we did not include biocytin for other experiments, we could not identify whether the recorded cell was one of the three HS cell types. However, no obvious differences were observed in the physiological responses in individual recordings. The stripe pattern turned for 1 s each CW (PD) or CCW (ND) direction at 1 Hz of temporal frequency, which is near the optimal frequency for *Drosophila* tangential cells (Schnell et al., 2010; 2014). A total of 12 motion patterns were presented in a pseudorandom order. The same stimulation pattern was given at least eight times for each cell.

2-2-5 Immunohistochemistry

Figure 3 shows the visualization of a biocytin-filled neuron. After recordings, the brain was fixed with 4% paraformaldehyde for 30 min at 4°C

and washed three times with PBST (0.1 M phosphate-buffered saline containing 0.2% Triton X-100). It was blocked with 5% normal goat serum (NGS) for 1 h and then incubated with a primary antibody solution containing 1:30 mouse anti-nc82 (Hybridoma Bank, Iowa City, IA, USA) at 4°C for 2 days. After washing with PBST, the brain was incubated with a secondary antibody solution containing 1:200 goat anti-mouse Alexa 633 and 1:500 streptavidin Alexa 555 (Molecular Probes, Eugene, OR, USA) at 4°C for 2 days. After washing with PBST, it was mounted in 400 µl Vectorshield (Vector Laboratories, Burlingame, CA, USA). Confocal images were acquired with an Olympus FV1000D IX81 confocal laser scanning microscope under 40× magnification.

2-2-6 Computer simulations

I constructed the 2-Quadrant-Detector model (Eichner et al., 2011) to reproduce HS activities in response to wide-field noisy motion stimuli. Reportedly, this model can semi-qualitatively reproduce a variety of

experimental data measured from *Drosophila* tangential cells (Eichner et al., 2011; Joesch et al., 2013).

To synthesize visual stimuli for the model, I needed to estimate how the image of the LED display device is projected onto the fly retina. As shown in Figure 5, the retinal projected image is calculated from the actual geometric arrangement of the LED display device. In each frame of the synthesized visual stimuli, the luminance of each pixel is represented by a dimensionless integer value ranging from 0 to 5. The image of each frame is filtered by a 2D Gaussian function with a 7.5° deviation of standard to mimic the receptive fields of lamina cells, which are formed by lateral inputs from different retina cells of six neighboring ommatidia (Sanes and Zipursky, 2010). After spatial filtering, the filtered signal is passed through a sigmoid transfer function that represents typical non-linear properties including cell membrane potential responses, synaptic transmission, and habituation to stimuli in the fly's visual system. I used the sigmoid transfer function defined as $f = \frac{K}{1+e^{a(I-I_0)}}$, where I is the filtered signal, K is a scaring factor,

I_0 is a threshold, and a is a gain. The parameters of this function were estimated by manual fitting to the results illustrated in Figure 3 ($K = 5$, $a = 2$, $I_0 = 2.5$).

The sigmoid output was processed by the 2-Quadrant-Detector model composed of a 2D motion detector array, which consisted of two subunits of horizontal and vertical local motion detectors located at lattice points in the 2D-array. Figure 5a shows the architecture of each motion detector. In Figure 5a, HP is a temporal first-order high-pass filter ($\tau = 250$ ms), and DC is a direct connection that passes 10% of the original signal. The sum of these is passed through two kinds of half-wave rectifiers that mimic the response properties of L1 and L2 cells (Joesch et al., 2010; Maisak et al., 2013). The ON and OFF pass-ways correspond to the L1 and L2 cells in the lamina, respectively. Note that a clip point of OFF pass rectifier slightly shifted to positive 0.05 with reference to Eichner et al. (2011). Therefore, the OFF pass-way signal involves a small amount of the ON signal. The outputs of the rectifiers are sent to the next process stage composed of the standard

Reihardt model (EMD), which consists of a first-order low pass-filter (τ = 150 ms), a multiplication, and an imbalanced subtraction (The positive:negative ratio is 1.0:0.8). The parameters of this stage were also estimated by manual fitting to the results illustrated in Figure 3. Compared to the parameters used in Eichner et al. (2011), the time constant of the low-pass filter is slightly larger, and the negative proportion in the imbalanced subtraction is slightly smaller. If I select the parameters used in Eichner et al. (2011), the model's residual activity after PD stimulation and ND stimulus response are not matched to our experimental results.

Tangential cells spatially integrate the output of local motion detectors on their dendrites and have receptive fields with a characteristic sensitivity distribution (Huston and Jayaraman, 2011; Krapp, 2009). To keep the model relatively simple, the receptive field was approximated by the weighed summation of the horizontal and vertical local motion detector outputs. The membrane potential of the model, V , was determined by the following formula:

$$V(t) = A\{Output_{horizontal}(t)w_h + Output_{vertical}(t)w_v\} + n(t),$$

where $Output_{horizontal}$ and $Output_{vertical}$ are the outputs of the horizontal and vertical local motion detectors, and w_h and w_v denote the weights of the horizontal and vertical components, respectively. $n(t)$ denotes a fluctuation of membrane potential described as follows. Figure 5b shows a vector field of the weight vectors $[w_h, w_v]$ depending on the position, which were determined to reproduce the receptive field of the actual HS cell (Krapp et al., 2001). A is a scaling factor, which was determined as A = 0.004.

To reproduce the fluctuation of membrane potential observed at the HS cells, I added a colored noise to the model output. I generated the colored noise signal using a first-order autoregressive (AR) model expressed as: $n(t) = n(t-1) + e_t$, where $n(t)$ is the noise at time t, j is a damping parameter determining the correlation length of the generated noise, and e_t is a white noise with variance σ^2. I recorded the spontaneous membrane activity of the HS cell for 5 s and estimated these parameters by fitting to the spontaneous activity with the Yule-Walker method. The estimates of these

are j = 0.9974 and σ^2 = 0.0022, respectively. Numerical simulations were carried out with MATLAB (MathWorks, Inc., Natick, MA, USA).

2-2-7 Data analysis

To quantify the behavioral and neuronal discrimination performances between PD and ND, I obtained histograms of both head yaw rotation and HS cell membrane potential in response to PD and ND motion stimuli and calculated ROC curves for the PD and ND response histograms. In the behavioral experiments, the histograms in Figure 2a to certain stimuli were calculated from data in the last 4 s during stimulus presentation for all flies. For electrophysiology, the histograms in Figure 3e were calculated by data from all trials in each cell. To cancel the variance in each trial, I subtracted the baseline from the raw data in each trial for both the behavioral and electrophysiological experiments. I defined the baseline as the average head yaw angle during the total experimental time in each trial and defined it as the average membrane potential in the 5 s before motion

stimuli onset in each electrophysiological trial.

Then I calculated the area under the ROC curve (AUC). Because the AUC is mathematically equal to the probability of getting the correct answer in a two-alternative forced choice test, it is a good indicator for quantifying the discrimination performance. When the ROC curve lies along the diagonal, the AUC is 0.5, suggesting that the fly cannot distinguish between two directions. When the ROC curve hugs the left axis and upper limit, the AUC approaches 1.0, indicating that the fly can fully distinguish between the two directions. These calculations were carried out with the Perfcurve function of MATLAB.

2-3 Results

2-3-1 Robust perception of wide-field motion with strong noise

I tested the OMR to motion stimuli with a computer-controlled LED display (Figure 1a). As shown in Figure 1b, flies turn their head to the direction of motion during the stimulus presentation. In order to quantify the response, I measured the head yaw angle, which was been established as an index of the OMR (Duistermars et al., 2012; Kikuchi et al., 2013; Zhu et al., 2009). To test the effects of reduced reliability of stimuli on wide-field motion perception, we need to precisely control a signal-to-noise ratio (SNR) of motion in the stimulus. Therefore, horizontally rotating vertical stripes superimposed with several intensities of random dot noise were used as the motion stimuli. The pattern was turned in clockwise (CW) and counter-clockwise (CCW) directions. I used two different temporal frequencies (1 and 4 Hz, Figure 1c and see Materials and Methods).

I evaluated the head yaw response over a range of SNRs (Figure 2). Flies obviously react to motion stimuli including substantial amounts of noise

(SNR = 3.274) at both temporal frequencies. However, when the SNR of the stimulus <3.274, flies no longer react (Figure 2a). In order to quantify how accurately flies could discriminate the two directions of the moving stimuli, I showed distributions of the head yaw response during the stimulus presentation (Figure 2 bottom panel and see Materials and Methods) and applied a ROC analysis to these distributions. The ROC analysis is a classical and commonly used method to evaluate the performance of perceptual detection, and it allowed us to directly and quantitatively compare the discriminative capacity of the behavior to that of the neural activity (Britten et al., 1992). The distributions of head yaw responses to CW or CCW motion directions are separate until SNR reached a moderate level (SNR = 5.006), and these two distributions became closer with an increase in noise. When the SNR reaches the strongest noise level, the distributions were no longer distinguishable (right, Figure 2a). As a result, the deflection of the ROC curves away from the diagonal until the moderate noise level (SNR = 5.006) and approaches the diagonal with increasing noise levels

(Figure 2b). Next, we calculated the area under the ROC curve (AUC). At both temporal frequencies, the AUC value remained with the value under stripe pattern until the critical noise level and then rapidly decreased (Figure 2c). These results indicate that flies can correctly discriminate rotating wide-field motion directions even though the SNR of the motion stimulus is quite low.

2-3-2 HS cell activities

To investigate the neural basis underlying the robustness of the OMR, I recorded membrane potentials of HS cells to wide-field motion stimuli with noise using a whole-cell patch clamp technique (Figure 3a). As reported previously, I also observed that HS cells depolarized or hyperpolarized during the presentation of an ipsilateral front-to-back preferred direction (PD) or back-to-front null direction (ND) horizontal motion stimulus, respectively (Figure 3d). PD motion stimuli elicited increases in membrane potential, including spike-like transient

depolarization. These spike-like changes in membrane potentials were often elicited by the moving patterns we used (see Materials and Methods). As indicated in Figure 3e, I presented flies with a rotational motion of the same range of SNR as used in our behavioral experiments described above with 1 Hz temporal frequency. The amplitude of membrane potential changes in response to PD motions decreased with an increase in the noise level (Figure 3e). To quantify the discriminative performance of HS cell activities, I analyzed the distributions of HS cell membrane potentials from which baseline amplitude was subtracted during the stimulus presentation and computed the ROC for each pair of two distributions (Figure 3e, bottom panel, and 3f). The ROC curve rises rapidly from the origin in Figure 3f until the moderate noise level (SNR = 5.006) because there is minimal overlap in the two distributions of membrane potentials in response to PD and ND motion stimuli. However, when the SNR of stimulus decreases, the ROC curve rises more slowly and approaches the diagonal because the distributions are overlapping. The value of AUC kept with the value under

the stripe condition until the moderate noise level and the rapidly decreases (Figure 3g). It was remarkably similar to the robust performance of the behavioral response (Figure 2c and 3g).

However, I found that HS cells' response to noisy motion stimuli was proportionally reduced with increased noise intensity (Figure 3h and i). Considering the spike-like response, the analysis based on the mean amplitude of membrane potential changes during stimulation was not appropriate to quantify HS cell response in our case. Therefore, I analyzed the response by integrating a baseline-subtracted mean membrane potential during motion stimulus presentation. The responses to both PD and ND motion increased with increasing SNR (Figure 3h). In addition, the differences between responses to PD and ND stimuli (mean response difference, MRD) linearly decreased with a greater noise level (Figure 3i). These results indicate that HS cells can robustly discriminate wide-field motion directions even though the stimulus contains considerable amount of noise and MRD was easily affected by noise. The behavioral discriminative

capacity can be accounted for by the neuronal discriminative capacity.

2-3-3 Effects of binocular vision

Previous studies have reported that binocular integration of wide-field motion via interhemispheric couplings modulates the flow field selectivity of LPTCs in blowflies (Farrow et al., 2006; Haag and Borst, 2001; Horstmann et al., 2000; Krapp et al., 2001; Suzuki et al., 2014). It is considered that LPTC activity in response to wide-field motion is influenced by binocular visual input. Therefore, binocular visual input might be necessary to produce the two distinct features of HS activity: robust discriminative capacity and MRD proportionally reduced with increased noise. To examine this view, I recorded HS cell activities while covering the opposite compound eye with a barrier that interrupted visual inputs (Figure 4a). Figure 4b shows the average membrane potentials of HS cells to motion stimuli under covered and uncovered conditions over the same of SNR as used in Figures 2 and 3. I found no significant differences between the

activities of HS cells recorded under both conditions in response to the wide-field motion stimulus (Figure 4b). Furthermore, there were no significant changes in the AUC or MRD of HS cells' response to motion stimuli under the covered condition compared to the uncovered condition (Figure 4c–e). These results indicate that ipsilateral visual inputs are sufficient to generate the distinctive features of HS activities in response to noisy motion stimuli.

2-3-4 Neural algorithms underling robust motion perception

Next, I focused on neural architectures and implementations underling HS cell coding. To address this problem, I used a mathematical modeling approach and used an elementary motion detector (EMD) model that is thought to reproduce LPTCs activities in facing wide-field motion stimuli (Borst et al., 2010; Reichardt, 1987). In this study, I built a spatial filter and sigmoidal threshold function into the EMD model (Figure 5a). The spatial filter was added to represent the receptive field properties of lamina

cells. The sigmoidal function was used to represent typical non-linear properties of neural cell membrane potential and synaptic transmission in the fly visual system. As indicated in Figure 5c, my model was applied to both PD and ND motion stimuli over the same range of SNR as in our experiments described above. The activities of HS cells observed in our experiments were successfully reproduced by our model simulations. To demonstrate the effectiveness of the spatial filter and threshold function, I compared the performance of models with and without these components. To quantify the discrimination performance of these different cases, I computed the AUC. The AUC of the model with both components kept with the value under the stripe condition until the critical noise level and then rapidly decreased as observed in the real HS activities (Figure 5d). The model with either one of the components was more sensitive to noise than the model with both modifications. Next, to investigate how the MRD of these models was affected by the increase in noise, I normalized MRD against that to the stripe. As shown in Figure 5e, in the models with threshold function only or

with spatial filter only, the normalized MRD values markedly fell as the SNR decreased. However, the model with both modifications qualitatively reproduced the normalized MRD value in the experimental result as a function of the SNR. Thus, the model with the spatial filter and threshold function accurately reproduced HS cell activities elicited by motion stimuli with random dot noise.

2-4 Conclusions and Discussion

Robust and reliable behavioral performance in a noisy environment and the underlying neural mechanisms have been attractive subjects for studying the function of the neural system. A number of studies of the visual system have focused on robust information processing by investigating the effects of photon and motion noise (Grewe et al., 2003; 2006; Warrant, 2004). These studies mainly observed the effects of noise on either behavioral aspects or neural activity. Few studies investigated both behavior and the underlying neural activity, although primate studies reported effects of the motion-noise on motion perception and neural activity (Britten et al., 1992; Newsome et al., 1989). However, because of the huge number of neural cells and the complexity of the primate neural system, it might be difficult to uncover the precise response properties of the behavior and its relationship with neural activity in such a large brain.

Here, I investigated the discriminative capacity of panoramic motion direction embedded in random dot noise with regard to both behavior

and neural activity levels in the tiny *Drosophila* brain. I showed the robust ability of flies to discriminate wide-field motion directions under considerable amount of noise (Figure 2). Moreover, the discriminative capacity of HS cells for moving direction strongly correlated with these behavioral performances of the OMR (Figure 3). This robust discriminative capacity of HS cells could only be revealed by ROC analysis because the membrane potential changes of the HS cells were proportionally reduced with increased noise. Our results provide the first evidence that a fly, which has a tiny brain, can correctly and robustly react to motion stimuli buried in noisy outside environment at both behavioral and neural levels.

I demonstrated that the neural network in the fly's tiny brain was sufficient to robustly respond to wide-field motion stimuli with strong noise. To clarify the neural and computational mechanisms underlying the robustness, I studied the impact of binocular integration on HS cell activity in response to motion stimuli with noise. There were no significant changes in HS cell activity between binocular and monocular motion stimulation

(Figure 4), indicating that ipsilateral visual input is sufficient to generate the distinctive HS activities to motion stimuli with noise. This finding is noteworthy because several studies have shown the necessity of binocular integration of LPTCs network for stimulus selectivity (Haag and Borst, 2001; Horstmann et al., 2000; Krapp et al., 2001). Conversely, HSE cells are much less affected by contralateral input (Farrow et al., 2006), which is consistent with our result. The response properties of HS cells might be minimally influenced by contralateral input because of their positions in the LPTCs network and their membrane properties.

Furthermore, I investigated neural architectures and implementations in HS cell coding with a mathematical modeling approach. In general, the local motion detector model is highly influenced and vulnerable to local noise in motion stimuli because it extracts motion information from temporal patterns of light intensity at adjacent locations within narrow regions. Therefore, the local motion detector model severely underestimates the response to motion stimuli with noise (Verghese et al.,

1999; Watamaniuk et al., 1995). In order to elucidate which mechanisms facilitate the noise-robust discriminative performance of HS cell activities, I added a Gaussian spatial filter and imaginary threshold function to the local motion detector model. We successfully reproduced the experimental results when we added a spatial filter and threshold function to the EMD model (Figure 5). These results suggest that spatial filtering and binarization of visual inputs are essential to generate the distinctive features of HS cell activities elicited by motion stimulus with noise. The spatial filter smoothed the stochastic signal fluctuations with a weighted average and reduced the contrast of visual patterns, while the threshold function emphasized and reconstructed the contrast reduced by spatial filtering. Thus, I think that smoothing out noise and contrast enhancement, which are accomplished by these two components, improve the SNR of visual inputs, which allows our model to account for the response properties of HS cells to noisy motion stimuli. With regard to the response of LPTCs, (Schnell et al., 2010) showed that the response amplitudes of HS cells to PD motion saturated when the

visual pattern contrast was high. In this study, I also observed the saturated response to the high SNR stimulus. The saturation property of the threshold function in our model is also required to explain the response properties of HS cell activity.

What are the physiological entities of these two components in the real fly visual system? Lamina monopolar cells are one candidate for the spatial filter. In *Drosophila*, one lamina cell receives visual channel outputs from six neighboring retina cells (Sanes and Zipursky, 2010) and seems to be involved in spatial summation. It is well known that in the visual systems of animals living in dark habitats, several interneurons and ganglion cells, each of which has a wide dendritic field, achieve spatial summation to improve visual performance in dim light conditions (Warrant, 1999). For the threshold function, candidates in the fly visual system would have typical properties of neural cells, such as non-linear neural responses to light intensity and non-linear synaptic transformation (Belusic et al., 2010; Juusola and Hardie, 2001; Juusola et al., 1996). Further anatomical and

functional analysis of motion visual networks will shed light on the physiological mechanisms of these two components.

Previous studies have demonstrated that HS cells in fact control the OMR (Blondeau, 1981; Haikala et al., 2013; Heisenberg et al., 1978). Recently, Haikala et al. (2013) showed that optogenetic activation of HS cells located in one hemisphere of the brain elicited a head yaw response in *Drosophila*, suggesting that HS cell activity is sufficient to evoke this response. However, the precise quantitative relationship between changes in the membrane potential of HS cells and the OMR had been poorly understood. In this study, I showed that the membrane potential changes of HS cells in response to noisy motion stimuli showed proportional reductions with an increase in noise intensity, that is, it dose not resemble the noise-robust discriminative performance of the OMR to the same stimuli. One possible explanation for this discrepancy is that synaptic outputs of HS cells could have different dynamics from the membrane potential of cell bodies. It was recently reported that the change in HS cell membrane

potential disagrees with the behavioral flight turning responses, but the calcium accumulation in its terminal is consistent with the behavioral response (Schnell et al., 2014). They also proposed that this accumulation provide a mechanism for temporal integration of sensory input. Their results imply that the calcium level in terminal is not proportional to its membrane potential changes. Further, there is a linear relationship between calcium level in terminals of VS cells and postsynaptic spike rates in V1 cells in the blowfly (Kurtz et al., 2001). Presumably, non-linear and noise-robust neurotransmitter release depending on presynaptic calcium levels might linearly modulate the postsynaptic spike rate. Such molecular mechanisms might provide the robust OMR to noisy motion stimuli.

In this study, I used ROC analysis to quantify the discriminative capacity instead of other statistical values, such as the mean of head turning angles or the mean of membrane potential changes. With this approach, I was able to show the robust discriminative performance to noisy stimuli and quantitatively compare neural activity with behavior. ROC analysis is

commonly used to directly compare neural activities and psychophysical decisions in primates (Britten et al., 1992). Previously, correspondence between neural activities and behavioral or psychophysical judgments has been also reported for the two-alternative forced choice test of stochastic motion stimuli in macaque monkeys (Britten et al., 1992; Newsome et al., 1989). These results are qualitatively similar to ours. Unlike primates, the precise neural network of the *Drosophila* visual system has been morphologically and functionally identified, so I was able to apply physiological approaches such as whole-cell recording *in vivo*. Due to the relatively small number of neurons compared to primates and the abundance of helpful genetic tools, *Drosophila* provides an ideal model system to investigate the detailed neuronal mechanisms underlying the processing and representation of unreliable information and its transformation to appropriate psychophysical decisions. Further research on robust perception in both vision and other sensory modalities, such as olfaction and audition, would enhance our understanding of the neural mechanisms required to

achieve robust information processing in the brain.

3 Effects of binocular integration on ego-motion estimation

3-1 Ego-motion

For many living beings, binocular visual perception is one of the most important functions of their visual systems. For example, the retinal images in the eyes are slightly different from each other, which is referred to as binocular disparity, and this difference provides information that the brain can use to calculate the depth of objects in the visual field. In monkey's visual cortex has been reported to have binocular depth neurons that are tuned to different ranges of binocular disparity (Hubel and Wiesel, 1970). Besides depth perception, visual ego-motion perception is an out standing function of binocular vision. For almost every animal, including vertebrates and invertebrates, ego-motion perception plays a dominant role in their motion control (Borst and Bahde, 1988; Jones, 1963; Kimmerle et al., 1996; Kirchner and Srinivasan, 1989; Reichardt et al., 1983). The direction of optic flow fields in the eyes depends on the type of ego-motion. Yaw-rotational motion of animals (rotational ego-motion) elicits two distinct optic flows

directed from front-to-back and from back-to-front on each eye. In contrast, forward or backward translation of animals (translational ego-motion) elicits an optic flow directed either from front-to-back or from back-to-front on both eyes. Motion stimuli caused by rotational ego-motion are referred to as in-phase motion stimuli, whereas ones caused by translational ego-motion are referred to as out-of-phase motion stimuli. Thus, the combination of optic flow fields in the eyes provides information that the brain can use to distinguish whether they are rotating or translating. To achieve this computation, motion information from the eyes has to be integrated in the brain.

3-2 Wide-field motion sensitive neurons

Motion-sensitive neurons that analyze optic flow fields and often have complex receptive fields are found at higher orders of processing in the visual systems of many species (Borst et al., 2010; Rauschecker et al., 1987; Schlotterer, 2011; Tanaka and Saito, 1989; Wylie and Frost, 1990). These

neurons are involved in the visual perception of orientation, locomotion tasks, and head movements. The neural mechanisms underlying optic flow analysis have been studied especially well in flies. In the visual system of the blowfly *Calliphoravicina*, there are the hierarchical structures consisting of four neuropils in the left and right hemispheres, and these neuropils retinotopically process motion information from the left and right eyes, respectively. After retinotopic processing, visual information converges in the lobula complex, which subsequently receive the signal processed by the medulla (Figure 6A). It contains a set of wide-field motion-sensitive neurons called lobula plate tangential cells (LPTCs) (Borst and Euler, 2011; Borst et al., 2010). LPTCs have complex receptive fields that cover a large part of the ipsilateral visual hemi-field and show directional-selective motion responses by shifting their membrane potential as well as evoking an action potential (Borst and Weber, 2011; Borst et al., 2010; Elyada et al., 2009; Farrow et al., 2005; Haag and Borst, 1997; Haag et al., 1997; 1999). Some of these cells have been also found in *Drosophila* (Fischbach and Dittrich, 1989; Joesch et

al., 2008). The LPTCs are grouped into horizontal and vertical cells that predominantly respond to horizontal (front-to-back or back-to-front) and vertical (upward or downward) motion stimulus on the ipsilateral visual hemi-field. The LPTCs include eight horizontal cells in each hemisphere of the blowfly's brain, of which three are named HS cells (HSN, HSE and HSS (Hausen, 1982)), two are named CH cells (dCH and vCH (Eckert and Dvorak, 1983; Gauck et al., 1997)), and the others are named Hu, H1 and H2 (Farrow et al., 2006; Haag and Borst, 2001; Horstmann et al., 2000). The H1, H2 and Hu cells are spiking neurons, whereas HS and CH cells are graded-potential neurons.

3-3 Bilateral network of wide-field motion sensitive neurons

Previous studies have identified the bilateral network of LPTCs (Farrow et al., 2006; Haag and Borst, 2001; 2003; 2002; 2008). It has been reported that the LPTCs make the intrahemispheric and interhemispheric connections and have the possibility to integrate the binocular motion

information in the network. Some of the horizontal LPTCs have been reported to have larger responses to in-phase motion than to out-of-phase motion (Eckert and Dvorak, 1983; Farrow et al., 2006; Haag and Borst, 2001; Horstmann et al., 2000; Krapp et al., 2001). Farrow et al. (2006) studied the cooperative behavior of H2 and contralateral HSE cells and demonstrated that an interhemispheric electrical coupling between the H2 cell and its contralateral HSE cell is an important factor in determining the sensitivity of the H2 cell to binocular motion stimuli. This was a pioneering study revealing that the response properties originated from not a single-cell behavior but a cooperative behavior with another LPTC in the network. However, whereas these studies focused on parts of the network, there has been no work as yet on cooperative integration of binocular motion performed by the whole LPTC network. Here, I reveal how the whole LPTC network works to integrate the binocular motion information and how the information are encoded by neural activity at all levels from a single cell up to the population of cells.

To address this problem, I took a mathematical modeling approach. It is technically difficult to record the membrane potentials of many cells simultaneously in vivo, and hence, it is difficult to ascertain data about the cooperative behavior of the whole network through measurements. However, it is possible to construct an accurate model of the bilateral LPTC network because a complete picture of its synaptic interactions has been experimentally identified. In this study, I focused on the network of horizontal LPTCs that mainly contributes to binocular motion integration and constructed a bilateral network model that takes into account all synaptic connections that have experimentally identified in the actual network.

First, I qualitatively reproduced the in-phase motion-sensitive response of the H2 cell that had been previously reported and made sure that it could be accounted for by the cooperative behavior of the bilateral network mainly via interhemispheric electrical coupling. I also found that the response properties of single H1 and Hu cells, unlike H2 cell, are not

influenced by motion stimuli in the contralateral visual hemi-field, but that correlations between these cell activities are enhanced by the in- phase motion stimulus. Next, to reveal the coding properties of a population of spiking LPTCs, I performed principal component analysis (PCA) on the firing rates of all spiking LPTCs. I showed that the two orthogonal patterns of correlated population activities given by the first two principal components represent the in-phase and out-of-phase motions, respectively, and the population activity is more sensitive to the in-phase motion stimuli. Furthermore, I found that these population-coding properties are strongly influenced by the interhemispheric electrical coupling. Finally, by reproducing these population-coding properties with a reduced model, I confirmed that the numerical results are not specific to the network model I constructed.

3-4 Materials and Methods

3-4-1 Fly visual system

The fly visual system consists of four neuropils called the lamina, medulla, lobula, and lobula plate that exhibit the same columnar structure as the retina and are retinotopically organized in both hemispheres. Visual motion information from each side of the visual field is retinotopically processed and converges on the lobula complex comprised of the lobula and lobula plate (Figure 6A). This complex contains a set of large motion-sensitive neurons, called lobula plate tangential cells (LPTCs). A total of 60 different cells exist in the blowfly, all of which show directional-selective motion responses by shifting their membrane potential as well as their action potentials (Borst et al., 2010). During preferred direction (PD) motion stimulation, the cells in each hemisphere are depolarized or generate action potentials, whereas during antipreferred or null direction (ND) motion stimulation, the cells in each hemisphere are hyperpolarized.

3-4-2 Bilateral horizontal LPTCs network

The LPTCs are grouped into horizontal and vertical cells that predominantly respond to horizontal and vertical motion stimuli, respectively. As mentioned above, I will focus on the horizontal cells. Each hemisphere consists of eight horizontal cells (Figure 6B). H1, H2 and Hu cells produce action potentials during PD motion stimulations (i.e., spiking cells). HS and CH cells respond to PD motion stimuli in a graded way (i.e., graded-potential cells). These horizontal LPTCs are mutually coupled through intrahemispheric and interhemispheric connections with various electrical and chemical synapses, as shown in Figure 6B. The experimental findings on these couplings have been reported in (Borst and Weber, 2011; Borst et al., 2010; Farrow et al., 2006; Haag and Borst, 2001). I constructed a network model of horizontal LPTCs by mainly referring to Borst et al. (2011).

3-4-3 Conductance-based model (Detailed model)

To keep the model relatively simple, I decided that the morphology of each model cell would be a simple long cylinder. Here, the model cells do not have dendritic branches as in the real cells. The HS and CH cells are modeled as one passive compartment (gray cylinders in Figure 6B), and the H1, H2 and Hu cells are modeled as one active compartment capable of producing action potentials (colored cylinders in Figure 6B). I ascertained that the behaviors of the single compartment model are much the same as the ones of the multi compartment model (data not shown). The morphological parameters of each model cell are listed in Table 1. The properties and distribution of ion-conductances in LPTCs are still unknown (but see also Haag et al., 1997; Torben-Nielsen and Stiefel, 2010). Thus, instead of high-dimensional conductance-based models, the type-I Morris-Lecar (ML) model is used to describe membrane currents in the active compartments. The ML model is one of the simplest conductance-based models capable of reproducing the variety of oscillatory

behaviors found in various excitatory membranes (Morris and Lecar, 1981). The ML model and simple passive model used here are uniformly described in terms of the following ordinary differential equations:

$$C_m \frac{dV}{dt} = -g_{fast} m_\infty (V - V_{fast}) - g_{slow} w (V - V_{slow})$$

$$-g_{leak}(V - V_{leak}) + I_{con} + I_{app} \qquad (1)$$

$$\frac{dw}{dt} = \frac{\phi (w_\infty - w)}{\tau}$$

where the conductances g_{fast}, g_{slow} and g_{leak} are for the fast, slow and the leak channels, respectively. Note that when g_{fast} and g_{slow} are zero, these equations are equivalent to a simple passive model. The passive electrical parameters including the leak parameters of the ML model are listed in Table 1. In this paper, the fast and slow channels are not specified as specific ion channels, whereas in the original ML model, the fast and slow channels are respectively calcium and potassium channels. The functions m_∞ and w are the equilibrium open fractions for the fast and slow channels, and t is the activation time constant for the slow channel. These functions are

$$m_\infty = 0.5[1 + \tanh\{(V - V_1)/V_2\}]$$

$$w_\infty = 0.5[1 + \tanh(V - V_3)/V_4]$$

$$\tau = 1/\cos\{(V - V_3)/2V_4\}$$

The parameters of the type-I ML model are listed in Table 2. I_{app} denotes the total postsynaptic current from motion-sensitive cells in the first-order neuropils (medulla and lobula), and I_{con} is the total postsynaptic current from the other horizontal LPTCs. A detailed explanation of I_{app} and I_{con} is given in the following subsections. Numerical simulations were carried out with the NEURON simulator.

3-4-4 Mimicking visual stimuli

I used four different binocular motion stimuli: clockwise(C), counterclockwise(CC), front-to-back(FB) and back-to-front(BF). The clockwise and counterclockwise motion stimuli are classified as in-phase horizontal binocular motion stimuli that are elicited when a fly rotates about

its vertical body axis (yaw). The front-to- back and back-to-front stimuli are classified as out-of-phase horizontal binocular motion stimuli that are elicited by forward and backward translation. By using these four motion stimuli, we can verify the response properties of the horizontal LPTCs network for all possible combinations of directions of stimuli for each eye. A simple way to simulate the responses of the LPTCs to the stimuli is to mimic the total postsynaptic current from the earlier neuropils, I_{app}, with either a depolarizing or hyperpolarizing DC current depending on whether each stimulus direction is preferred or not by each cell. In this way, $I_{app}$is determined by the following formula:

$$I_{app} = S_X + n$$

$$X = P \text{ or } N,\ \langle n(t)\rangle = 0,\ \langle n(t)n(t')\rangle = \sigma^2\delta(t - t')$$

where n is a white noise term independent from neuron to neuron and s is the noise intensity. S_X represents the DC signal that changes to S_P or S_N depending on whether each motion stimulus is PD or ND for each cell. The

cells with black arrows in Figure 6B receive projections from the first-order neuropils, and the direction of each arrow denotes the preferred direction of each cell. Table 3 shows the amplitude of the DC signal given to each horizontal LPTC. Note that the CH cells (not marked with black arrows in Figure 6B) do not directly receive projections from the earlier neuropils (Haag and Borst, 2001), and thus, S_X of the CH cells is set to zero. Table 4 shows all combinations of either depolarizing or hyperpolarizing current for representing the four stimuli.

To measure the robustness of neural coding, we define the signal to noise ratio (SNR) for I_{app} as

$$SNR = \frac{S_X}{\sigma}$$

I analyzed the responses of spiking LPTCs with various SNR.

3-4-5 Connection properties

To construct a network model of the horizontal LPTCs, I connect the conductance-based models through electrical and chemical synapses, as shown in Figure 6B. In Eq. (1), I_{con} denotes the total postsynaptic current from the other horizontal LPTCs. The implementation of I_{con} can be easily realized with the NEURON simulator. Electrical couplings can be implemented with the NMODL function of the NEURON simulator. This function makes a conductive connection between two connected compartments with a particular conductance. In this study, all electrical couplings have the same conductance (40 nS) (Farrow et al., 2006). The excitatory and inhibitory chemical synapses are modeled as a change in synaptic conductivities triggered by spike events in presynaptic cells, which are implemented using the ExpSyn function of the NEURON simulator. The reversal potentials of the excitatory and inhibitory synapses are 0 mV and -70 mV, respectively. The conductance of excitatory and inhibitory synapses is described by a simple exponential decay with a time constant of 0.3 ms and

amplitudes of 0.01 and 0.005 nS, respectively. I manually tuned these synaptic parameters to fit the simulated EPSP and IPSP to previously reported physiological data (Farrow et al., 2006; Haag and Borst, 2001).

As described above, the CH and HS cells are non-spiking. It has been reported that the CH cell inhabits the activities of the ipsilateral H1 and H2 cells, and the HS cell excites the activities of the ipsilateral Hu cell. In this study, the excitatory postsynaptic current depending on the presynaptic graded-potential is de- scribed using a sigmoid function,

$$f(V) = \frac{K}{1+e^{-\alpha(V-x_0)}} \qquad (2)$$

where V is the graded potential of the presynaptic neuron, i.e., the HS cell. The inhibitory postsynaptic current depending on the presynaptic graded potential is given by $-f(V)$. The parameters used in the simulations were K= 0.2nA, α= 0.4 and x_0= -47 mV.

The purpose of this study is to clarify the role of the bilateral horizontal LPTC network in the binocular motion integration. For this

purpose, I compared two cases: one in which the cells are mutually connected as described above, the other in which the cells are isolated from each other without lateral connections. In the following sections, I will refer to these cases as the connected case and disconnected case.

3-4-6 Formal neuron model (Reduced model)

To check the generality and robustness of the results obtained from the conductance-based model, I constructed a reduced model and verified whether or not it qualitatively reproduced the results. In this model, five graded-potential cells, which are coupled through electrical synapses and have similar response properties, are merged into a single neuron named HS/CH. Furthermore, I used McCulloch Pitts formal neurons instead of the conductance-based model. The state space equation for the reduced model is

$$\tau \frac{d\mathbf{V}}{dt} = \mathbf{I_{app}} + \mathbf{W}f(\mathbf{V}) + \mathbf{GV} - \mathbf{V} \qquad (3)$$

$$\mathbf{V} = (V_{H1L}\ V_{H2L}\ V_{HuL}\ V_{HSL/CHL}\ \ V_{H1R}\ V_{H2R}\ V_{HuR}\ V_{HSR/CHR})^{\boldsymbol{T}}$$

where ^{T} denotes matrix transposition, $\mathbf{V}$ denotes the state vector consisting of the membrane potentials of eight cells and t is the time constant (τ= 5 msec). $f(x)$ is the sigmoidal function defined in Eq. (2), which represents the transfer function of each cell. The matrix $\mathbf{W}$ represents the couplings between these cells through chemical synapses, and the matrix $\mathbf{G}$ denotes the electrical couplings between them. w_e and w_i in $\mathbf{W}$ are the weights of the excitatory and inhibitory synapses, respectively, and g in $\mathbf{G}$ is the conductance of the electrical couplings. Thus, each component of the vector $\mathbf{W}f(\mathbf{V}) + \mathbf{GV}$ describes the total postsynaptic current in each cell via lateral connections.

The vector $\mathbf{I}_{app}$ in the state space equation denotes the input vector in which each component represents the total postsynaptic current of each cell from motion-sensitive cells in the earlier neuropils. As described in the detailed model, to simply simulate responses of the LPTCs to the four types of stimuli, $\mathbf{I}_{app}$ is mimicked with a combination of depolarizing or

hyperpolarizing DC currents depending on whether each stimulus direction is preferred or not by each cell. $\mathbf{I}_{app}$ is given by

$$\mathbf{I}_{app} = \mathbf{S}_X + [n_1\ n_2\ \cdots\ n_8]^T$$

$$X = In \text{ or } Out,\ \langle n_i(t)\rangle = 0,\ \langle n_i(t)n_j(t')\rangle = \sigma^2\delta(t-t')\delta_{i,j}$$

where n_i are white noise term independent from neuron to neuron and σ is the noise intensity. $\mathbf{S}_{In}$ and $\mathbf{S}_{Out}$ are the input vectors when presenting in-phase and out-of-phase stimuli:

$$\mathbf{S}_{In} = [s\ s\ -s\ -s\ -s\ -s\ s\ s]^T$$

$$\mathbf{S}_{Out} = [-s\ -\ s\ s\ s\ s\ -s\ -\ s]^T$$

where s is a time-dependent variable taking +1 or -1. If s=1, the input patterns of $\mathbf{S}_{In}$ and $\mathbf{S}_{Out}$ correspond to clockwise rotation and forward translation motion stimuli, respectively, whereas if s=-1, the input patterns of $\mathbf{S}_{In}$ and $\mathbf{S}_{Out}$ correspond to counterclockwise rotation and backward translation motion stimuli, respectively.

The parameters for the formal neuron model used in the simulations were g=1, w_e=1, w_i=-1, α=0.5, x_0=0.5 and K=5. The simulations were carried out with MATLAB.

3-4-7 Data analysis

Cross-correlation analysis

Let x_n and y_n be the mean firing rates of different cells at time n. The cross-correlation between x_n and y_n is defined as

$$R(\tau) = \sum_{n=0}^{N-\tau-1} x_{n+\tau}\, y_n$$

where N is the length of these two sequences and t is a time lag. For the cross-correlation analyses, the mean firing rate was calculated at intervals of 10 msec.

Principal component analysis of multi-neuronal activity

The principal component analysis (PCA) is a dimensionality reduction technique in which high-dimensional data is linearly projected on an orthogonal subspace spanned by vectors representing highly correlated directions (Jolliffe, 2005). I tried to elucidate the correlated activities of a neural population coding the four types of binocular motion stimuli by applying PCA to simulated multi-neuronal activity data. First, I calculated the mean firing rates of six spiking LPTCs at intervals of 150 msec within non-overlapping 150 msec temporal windows, and I constructed a set of six-dimensional firing rate vectors, $\overrightarrow{g_1}$, $\overrightarrow{g_2}$, . . . $\overrightarrow{g_T}$, where T denotes the total number of firing rate vectors (e.g. T=160 when the length of the spike sequence is 24 sec). Next, I performed principal component analysis (PCA) on the set of the firing rate vectors. The calculation was carried out with the princomp function of MATLAB.

3-5 Results

3-5-1 Modification of H2 cell by contralateral LPTC activities

I carried out numerical simulations of the detailed model (see Material and Methods for details) to analyze how the activity of single LPTCs of one hemisphere in response to the PD motion stimulus presented in the ipsilateral visual hemi-field are modified by changes in the contralateral LPTCs activities depending on motion stimuli in the contralateral visual hemi-field. I focused on three spiking LPTCs in the left hemisphere, H1L, H2L and HuL. The H2L cell is directly connected with the HSE cell of the right hemisphere through an interhemispheric electrical coupling, and the H1L and HuL cells indirectly receive effects from the contralateral cells via other ipsilateral cells (see Figure 6B). Note that it is not necessary to show the activities of counterparts of these three cells in the right hemisphere. This is because the bilateral LPTCs network has a reflective symmetric structure, statistical response properties of LPTCs separately located on both hemispheres to pair of binocular motion stimuli

which are in symmetric relation are the same. Therefore, it is sufficient to check for the responses of LPTCs located on one hemisphere.

To quantify the effect of the connections among LPTCs on the activities of each spiking LPTC, I compared the disconnected case and the connected case, as described in Materials and Methods section. In the disconnected case, I numerically simulated the responses of single spiking LPTCs isolated from other cells to the PD motion stimulus only presented in the ipsilateral visual hemi-field. In the connected case, I numerically simulated the responses of single spiking LPTCs to the in-phase and out-of-phase motion stimuli.

Figure 7A shows the spike raster plots displaying the spike times of the H2L cell in these cases, and Figure 7B show the difference of the mean firing rate from spontaneous activity in the H2L cell as a function of the signal-to-noise ratio (SNR) (defined in Materials and Methods). I found that the difference in mean firing rate induced by the clockwise motion in the connected case is lager than in the disconnected case. In contrast, the

difference in mean firing rate induced by the back-to-front motion in the connected case is smaller than in the disconnected case. Figure 7C shows the distributions of inter-spike intervals (ISIs) of the H2L cell. The ISI distribution for the clockwise motion in the connected case is sharper than in the disconnected case, whereas the ISI distribution for the back-to-front motion in the connected case is broader than in the disconnected case. Therefore, though, in all these cases, the H2L cell faces the same PD motion stimulus in the ipsilateral visual hemi-field, the activity and regularity of the H2L cell are modified by the chenges in the contralateral LPTCs activities depending on motion stimuli in the contralateral visual hemi-field. Moreover, to investigate the contribution of interhemispheric electrical couplings between the H2 cell and contralateral HSE cell to the selectivity of the H2 cell, I removed the interhemispheric electrical couplings from the detailed model and simulated the response of the H2L cell similarly to the above. As shown in Figure 7D and Figure 7E, the differences in mean firing rate and the ISIs of the H2L cell are not altered by the type of binocular

motion in this situation. Therefore, I consider that the interhemispheric electrical coupling is a key factor in determining the responsive characteristics of the H2 cell to binocular motion stimuli. My numerical results are in accord with *in-vivo* experimental results indicating that the H2 cells are more activated by an in-phase motion stimulus than by an out-of-phase motion stimulus (Farrow et al., 2006).

3-5-2 Enhancement of synchronization between spiking LPTCs in the in-phase motion

In the previous subsection, I focused on modifications of single-cell activities depending on contralateral motion stimuli. Here, I tried to determine whether a combination of motion stimuli presented in the left and right visual hemi-fields affects the synchronization between spiking LPTCs. For this purpose, I calculated the cross-correlation between the firing rates of two spiking LPTCs (see Materials and Methods for details).

Figures 8A and B show the cross-correlation between the H1L and H2L cells located in the left hemisphere when presenting clockwise and back-to-front motion stimuli, respectively. In both these cases, each of the cells is exposed to the PD motion stimulus in the left visual hemi-field. When the two cells are exposed to the clockwise motion stimulus, the peak of the cross-correlation at a lag of 0 msec is higher than the peak that occurs with the back-to-front motion stimulus. This is because the out-of-phase motion stimulus decreases both the firing rate and regularity of the H2 cell (see Figure 7).

Figure 8C shows the cross-correlation between the H1L and HuR cells separately located in the two hemispheres when presenting the clockwise motion stimulus, and Figure 8D shows the cross-correlation between the H1L and H1R cells separately located in the two hemispheres when presenting the back-to-front motion stimulus. In both cases, each cell is exposed to the PD motion stimulus presented in the ipsilateral visual hemi-field. Thus, as shown in Figure 9 and Figure 10, these cells have

identical differences in mean firing rate from the spontaneous activity and identical ISI distributions. However, as shown in Figure 8C and Figure 8D, the peak of the cross-correlation between the firing rates of the H1L and HuR cells at a lag of 0 msec when presenting the clockwise motion stimulus is slightly higher than that of the cross-correlation between the firing rates of the H1L and H1R cells when presenting the back-to-front motion stimulus. Therefore, the synchrony of these cells is enhanced by the in-phase motion stimulus. The numerical results suggest that the H1 and Hu cells, whose single-cell activities are independent of the motion stimuli presented in the contralateral visual hemi-field, could represent information on the binocular motion stimuli through their synchrony.

3-5-3 Synchronous activities of the bilateral network represent binocular stimuli

In the previous subsections, I examined the modifications of the single-cell activities and synchronies in spiking LPTCs in relation to binocular motion stimuli. Here, I use principal component analysis (PCA) to

reveal the properties of population activities of spiking LPTCs in response to four different motion stimuli. First, I calculated the mean firing rates of six spiking cells and construct a set of six-dimensional firing rate vectors (see Materials and Methods for details). Then, by applying PCA to the set of firing rate vectors, I projected them onto a two- dimensional space spanned by the first and second principal components, PC1 and PC2. PC1 and PC2 were found by calculating the two eigenvectors associated with the first- and second-largest eigenvalues of the correlation matrix obtained from the firing rate vectors. Thus, the principal components represent highly correlated or synchronous activity patterns of the spiking LPTCs. This analysis incorporated the correlation analysis carried out in the previous subsection.

The upper and lower parts of Figure 11A show examples of simulated spike sequences of six spiking LPTCs (denoted by raster plots) in the disconnected and connected cases for four different motion stimuli. Figure 11B shows the results obtained by applying PCA to these simulated spike sequences. In the disconnected case, four clusters of firing rate vectors

corresponding to four different stimuli are respectively separated into the four quadrants in the PC1–PC2 space (left panel in Figure 11B). Clusters corresponding to the clockwise and back-to-front motion stimuli are distributed within the right half plane of the PC1–PC2 space. These two stimuli share the same visual motion in the left visual hemi-field. On the other hand, the clusters of the counterclockwise and front- to-back motion stimuli are distributed within the left half plane of the PC1–PC2 space. These two stimuli also share the same visual motion in the left visual hemi-field. Therefore, PC1 represents a population activity coding the left monocular visual motion. In the same way, each pair of clusters distributed within the upper or lower half plane of the PC1–PC2 space corresponds to the same visual motion in the right visual hemi-field. Thus, PC2 represents a population activity pattern that codes the right monocular motions. This result is trivial because in the disconnected case, the cells are isolated from each other without lateral connections. Figure 12 shows the values of each element of PC1 and PC2 in five trials of numerical simulations with different

random seeds for noise, and it also presents what each principle component codes in the five trials. It shows that PC1 and PC2 are randomly assigned to either left or right monocular motion. Thus, there is no eye dominance in the disconnected case. In the connected case, on the other hand, two pairs of clusters corresponding to the in-phase and out-of-phase motion stimuli are distributed along the PC1 and PC2 axes, respectively (right panel in Figure 11B). Therefore, the PC1 and PC2 represent population activity patterns that code the in-phase and out-of-phase motions, respectively. I also found that PC1 and PC2 stably represent the in-phase and out-of-phase motions with different random seeds for noise (Figure 12). Figure 11C shows the contribution ratio of PC1 and PC2 and the cumulative contribution ratio in the connected and disconnected cases. The difference between the contributions of PC1 and PC2 in the connected case is larger than those of the disconnected case.

To check whether or not the neuronal morphologies affect on the coding properties, I carried out an additional simulation under conditions in

which the length of each LPTC is two-third that of the original model. I obtained the same results as those obtained by the original model (Figure 13). Therefore, I speculate that the neuronal morphologies do not strongly affect on the coding properties.

3-5-4 Effect of interhemispheric electrical couplings on population coding in the bilateral network

Here, I evaluated the effect of the interhemispheric electrical coupling between the H2 cell and contralateral HSE cell on population coding in the bilateral network. I carried out numerical simulations on the detailed model using several different conductances of the interhemispheric electrical coupling, and I applied PCA to the simulated spike sequences, as in Figure 11. I used four different conductances: 0, 33.3, 50 and 100 nS. The parameters used in this simulation, except for the electrical coupling, were the same as in the previous simulations.

As shown in Figure 14A, in the case of no electrical coupling (0 nS), four clusters of firing rate vectors corresponding to four different motion stimuli are respectively separated into the four quadrants of the PC1–PC2 space. This result conforms to that of the disconnected case shown in Figure 11B. Furthermore, as shown in Figure 14B, the difference in the contribution ratios of PC1 and PC2 is relatively small compared with those of the other nonzero cases, which is also similar to the disconnected case. When the electrical coupling between the H2 and HSE cells exists, two pairs of clusters corresponding to the in-phase and the out-of-phase motion stimuli are respectively distributed along the PC1 and PC2 axes (Figure 14A). The difference between the contribution ratios of PC1 and PC2 increases with the conductance of the electrical coupling (Figure 14B). These results suggest that the interhemi- spheric electrical coupling between the H2 and HSE cells strongly contributes to the coding properties of a population of LPTCs in the network.

3-5-5 Properties of population coding in the reduced model

To check whether or not the numerical results are specific to the network model I constructed, I construct a reduced model and tried to reproduce the results of Figure 11. To simplify the structure of the LPTC network, in each hemisphere, I merged five graded- potential neurons, which are coupled through electrical synapses, into a single neuron named HS/CH, as shown in Figure 15A. Furthermore, to simplify the activity properties of cells, I described all LPTCs in the network by using the McClloch-Pitts model instead of the conductance-based model (see Materials and Methods for details).

The left and right panels of Figure 15B show examples of the activities of three LPTCs corresponding to the spiking cells in the left hemisphere in response to the four different motion stimuli in the connected and disconnected cases. Figure 15C shows results obtained by applying PCA to a set of six-dimensional state vectors consisting of the responses of six spiking LPTCs in both hemispheres. In the disconnected case (left panel in

Figure 15C), four clusters of state vectors corresponding to four different motion stimuli are respectively separated into the four quadrants of the PC1–PC2 space, whereas in the connected case (right panel in Figure 15C), two pairs of clusters corresponding to the in-phase and the out-of-phase motion stimuli are distributed along the PC1 and PC2 axes. Figure 15D shows the contribution ratio of PC1 and PC2 and the cumulative contribution ratio in the connected and disconnected cases. The difference between the contributions of PC1 and PC2 in the connected case is larger than in the disconnected case. Figure 16 shows the values of each element of PC1 and PC2. The principal components of the reduced model qualitatively correspond to those of the detailed model. Therefore, the results obtained from the reduced model qualitatively conform to those of the detailed model in Figure 11.

3-6 Conclusions and Discussion

3-6-1 Summary of results and conclusion

I investigated the cooperative behavior of the LPTCs underlying the integration of binocular motion information and the information representation in the bilateral LPTC network through numerical simulations. First, I showed that the cooperative activities of cells in the bilateral network via interhemispheric couplings, especially interhemispheric electrical couplings, could account for the in-phase sensitive response of the H2 cells that was previously reported (Figure 7). Moreover, the results of cross- correlation analyses suggested that the other spiking LPTCs, H1 and Hu, might be involved in representing binocular motion in a manner that is a synchrony of these activities (Figure 8). I also applied PCA to the firing rates of all spiking LPTCs and found that when the LPTCs are isolated from each other; two orthogonal patterns of correlated population activities given by PC1 and PC2 represent the monocular motions, whereas when the LPTCs are connected to each other, two orthogonal

patterns of correlated population activities respectively represent the in-phase and out-of- phase motions, and the population activity is more sensitive to the in-phase motion stimuli (Figure 11). Moreover, I found that the inter- hemispheric electrical couplings strongly influence these population- coding properties (Figure 14). Finally, I confirmed the generality and robustness of these results by using a reduced model (Figure 15).

3-6-2 Intuitive explanation of the binocular motion integration

Let us try to intuitively understand the cooperative behavior of the LPTCs underlying binocular motion integration by referring to the reduced model. Figure 7 illustrates the activity patterns of the cells responding to the in-phase and out-of-phase motion stimuli and the synaptic connections of the network. In the case of the in-phase motion stimulus, the polarity of each cell depending on the PD motion matches the polarity of each lateral synaptic connection (Figure 17A), resulting in an enhancement of each cell's sensitivity to the PD motion. In this situation, cells cooperatively integrate

the motion information in the bilateral network. On the other hand, in case of the out-of-phase motion stimulus, the polarity of each cell depending on its PD motion is somewhat mismatched to the polarity of the lateral synaptic connections (Figure 17B and Figure 17C), resulting in a decrease in sensitivity. This mechanism can account for the increase in the response of some LPTCs during the in-phase motion stimulation reported in previous in vivo experiments (Eckert and Dvorak, 1983; Farrow et al., 2006; Haag and Borst, 2001; Horstmann et al., 2000; Krapp et al., 2001). Furthermore, it is known that mismatches between cell polarity and lateral synaptic polarity, which are referred to as frustration, induce asynchronous cell activities in a general class of networks. Thus, this mechanism can also account for the greater synchrony among LPTCs in response to in-phase motion compared with the response to the out-of-phase motion (Figure 8 and Figure 11).

3-6-3 Reliability of modeling with the ML model

Through in vivo experiments, Farrow et al. (2006) suggested the possibility that the interhemispheric electrical coupling between H2 and contralateral HSE cells is involved in the flow field selectivity of H2 cells. Moreover, they indicated through numerical simulations that the electrical couplings can quantitatively account for the selectivity of the H2 cell. In the simulations, they used a simplified neural network of the horizontal LPTCs, which consisted of four horizontal cells, H1, H2, HS and CH cells in each hemisphere. In contrast, my neural network model (the detailed model) has a more anatomically accurate structure, in which I modeled all of horizontal LPTCs that include cells ignored in Farrow et al. (2006). I demonstrated that the in-phase sensitive response of H2 cells can also be qualitatively reproduced by our detailed model and that it can be accounted for by the interhemispheric electrical coupling (Figure 7). My numerical results are consistent with the results of Farrow et al. (2006), and this consistency ensures the reliability of the results obtained from our model.

Farrow et al. (2006) used the Hodgkin-Huxley model for the spiking LPTCs. At present, however, the properties and distribu- tion of the ion-channels of spiking LPTCs are not well understood. Hence, the Hodgkin-Huxley model is not the only way to model spiking LPTCs. In this paper, I used the Morris-Lecar (ML) model for the spiking LPTCs in the detailed model. The ML model, which has a two-dimensional state space, shares a common bifurcation structure with other high-dimensional Hodgkin- Huxley type models classified into types I and II, and it can reproduce electrical responsiveness of typical neurons. Therefore (invoking Occam's razor), in circumstances where the properties of the membrane ion-conductances of the cell that we want to model are unknown, a lower dimensional model with high explanatory power should be used. However, in the ML model, the firing rate is limited to less than 30 Hz. The firing rate of the real spiking LPTCs, for example, the H2 cell, is more than 50 Hz, or even 100 Hz in some circumstances. Thus, the ML model cannot adequately reproduce the firing rate of spiking LPTCs. Despite this, the numerical

results obtained from the ML model qualitatively conform to results observed *in vivo* (Farrow et al., 2006; Haag and Borst, 2001). Moreover, as shown in Figure 6, I confirmed that the results of simulation are not dependent on the conductance-based model we used by testing the more simplified model consisting of McCulloch Pitts units. According to the consistent results obtained from the two models, we conclude that the spiking mechanism based on the properties of the membrane ion-channels do not affect properties of population coding in the network sensitively. Accordingly, I consider that the ML model is able to capture the mechanism of binocular motion integration.

3-6-4 Potential of synchronized coding of binocular motion in spiking LPTCs other than H2 cells

In the detailed model, I demonstrated that the firing rate and regularity of single H1 and Hu cells, unlike H2 cells, are not influenced by motion stimuli in the contralateral visual hemi-field (see Figure 9 and Figure 10). However, I showed that the correlations between these cell

activities are enhanced by the in- phase motion stimulus (Figure 8). From a structural viewpoint, there is a major difference between H2 and the other horizontal spiking LPTCs in the manner of their receiving inputs from the contralateral LPTCs. H2 cells directly receive input via the interhemispheric electrical coupling from the contralateral cell. Therefore, the activity of H2 cells is strongly influenced by the contralateral motion stimulus. H1 and Hu cells, on the other hand, indirectly receive input from the contralateral hemisphere via the ipsilateral graded-potential cells, and the input is not strong enough to change the firing rate or regularity. The spike timings of H1 and Hu cells are entrained with each other through the indirect and weak interaction, and this makes the correlation of the activities of these cells dependent on the binocular motion. It is theoretically conjectured that the weak interaction, which is too weak to change phase trajectories in oscillations, enhances the synchronization of spikes across neurons (Aonishi et al., 1999; Kuramoto, 2003). This result suggests that H1 and Hu cells, unlike H2 cell, represent the binocular motions by using not the individual

cell activity but the correlation of activities. Little is known about the responsivity of H1 and Hu cells to binocular motion. To reveal the representation of binocular motion in these cells, the responsivity of these LPTCs to binocular motion will have to be recorded electro-physiologically.

3-6-5 Significance of sensitive response to in-phase motion in OMR

What are the functional roles of the sensitive response to the in-phase motion? It has been reported that neurons sensitive to in-phase motion exist in other species, for instance, descending neurons ($DNVII_1$) in the honeybee (Ibbotson, 1991). It is also known that many species of insect, crustacean, and mammal have the ability to stabilize retinal images by moving their eyes, head or whole body to compensate for their movements through the environment (Borst et al., 2010; Kern and Varjú, 1998; Kern et al., 1993). This motor action is referred to as the optomotor response. It can be thought that the neurons sensitive to the in-phase motion provide the most important cue for the optomotor response, because retinal image

motions evoked by perturbed movements of the observer's head and body are the in-phase motion in most cases.

3-6-6 Importance of our analysis method

A large number of studies have sought to reveal the coding properties of neural populations by using simultaneous multi- neuronal recordings and statistical techniques (Georgopoulos et al., 1986; Lemus et al., 2007; Sasaki et al., 2007; Stopfer et al., 2003). However, there is a limit on the number of neurons that can be simultaneously recorded *in vivo*. Thus, I must infer the population-coding properties of a whole local network from partial data. The limitations of such a measurement make it hard to understand the population coding in the whole local network.

On the other hand, researchers are using advanced genetic tools to get a complete picture of synaptic interactions in the whole brain of the fly (Ito et al., 2013). If the synaptic interactions in local networks can be completely

identified, we can construct accurate models of these local networks. Then, by combining numerical simulations of the network model with statistical techniques, we can elucidate the population-coding properties of the whole local network. Moreover, by altering the conductance of a particular synapse in the network model, we can evaluate the contribution of the synapse to the information processing or representation of the network. In this paper, I showed that interhemispheric electrical couplings play a key role in the integration of binocular motion information. Although compared with chemical synapses, much less is known about how electric couplings contribute to information processing in a neural network, it has recently become recognized that the electric couplings play a significant role in information processing in the local network (Yaksi and Wilson, 2010). Present study provides an important clue to understanding the functional role of electrical couplings in visual information processing. Moreover, unlike multi-neuronal recording approaches, we can use this approach to answer a

big question about how the computation is implemented with neural interactions.

4 Summary

In this study, to address a neural basis of robust behavioral control in the natural environment, I investigated how noisy motion stimulus is processed to correctly detect the motion direction and to guarantee robust optomotor reactions in an early stage of fly visual system and how bilateral motion information is integrated for efficient estimation of an ego-motion in *Drosophila melanogaster*.

First, I revealed that flies are able to guarantee robust optomotor reaction to wide-field motion with random dot noise from behavioral experiments. To uncover its neural basis, I measured the activity of motion sensitive neurons, which might control the optomotor response. I found that membrane potential changes of motion sensitive neurons were not correlated with the behavioral reactions, however, interestingly, by applying signal classification theory to distributions of these neural response, I found that the motion direction with noise can be clearly discriminated by these neurons, which were quantitatively similar to that in the behavioral

optomotor response (Figure 2 and 3). Furthermore, I successfully reproduced these neural activities in response to noisy motion stimuli with the local motion detector model including a spatial filter and threshold function (Figure 5).

Second, I showed that the population activity of motion sensitive neurons is more sensitive to the in-phase than the out-of-phase motion stimuli from theoretical studies (Figure 11). This result indicates that flies became easily react to rotational wide-field motion stimuli than translational ones. Furthermore, I identified a key structure for the in-phase sensitive population activity (Figure 14).

From these two studies, I uncovered neural algorithms from robust detection of motion direction to robust control of behavioral reaction. I found that the robust motion sensation emerges from an early stage of visual system prior to the bilateral network and the network more efficiently encodes a rotational ego-motion than translational one by binocular integration. This study provides a physiological and theoretical basis for

robust behavioral control in the tiny brain, and will contribute to develop robust robot control.

References

Aonishi, T., Kurata, K., and Okada, M. (1999). Statistical mechanics of an oscillator associative memory with scattered natural frequencies. Phys. Rev. Lett. *82*, 2800–2803.

Belusic, G., Pirih, P., and Stavenga, D.G. (2010). Photoreceptor responses of fruitflies with normal and reduced arrestin content studied by simultaneous measurements of visual pigment fluorescence and ERG. J. Comp. Physiol. *196*, 23–35.

Beyeler, A., Zufferey, J. C., and Floreano, D. (2009). Vision-based control of near-obstacle flight. Auton Robot *27*, 201–219.

Blondeau, J. (1981). Electrically evoked course control in the fly *Calliphora Erythrocephala*. J. Exp. Biol. *92*, 143–153.

Borst, A., and Bahde, S. (1988). Spatio-temporal integration of motion. Naturwissenschaften *75*, 265–267.

Borst, A., and Euler, T. (2011). Seeing things in motion: models, circuits, and mechanisms. Neuron *71*, 974–994.

Borst, A., and Weber, F. (2011). Neural action fields for optic flow based navigation: a simulation study of the fly lobula plate network. PLoS ONE *6*, e16303.

Borst, A., Haag, J., and Reiff, D.F. (2010). Fly motion vision. Annu. Rev. Neurosci. *33*, 49–70.

Brand, A.H., and Perrimon, N. (1993). Targeted gene expression as a means of altering cell fates and generating dominant phenotypes. Development *118*, 401–415.

Britten, K.H., Shadlen, M.N., Newsome, W.T., and Movshon, J.A. (1992). The analysis of visual motion: a comparison of neuronal and psychophysical performance. J. Neurosci. *12*, 4745–4765.

de Belle, J.S., and Heisenberg, M. (1994). Associative odor learning in *Drosophila* abolished by chemical ablation of mushroom bodies. Science *263*, 692–695.

Duistermars, B.J., Chow, D.M., Condro, M., and Frye, M.A. (2007). The spatial, temporal and contrast properties of expansion and rotation flight optomotor responses in *Drosophila*. J. Exp. Biol. *210*, 3218–3227.

Duistermars, B.J., Gare, R.A., and Frye, M.A. (2012). Binocular Interactions Underlying the Classic Optomotor Responses of Flying Flies. Front. Behav. Neurosci. *6*.

Eckert, H., and Dvorak, D.R. (1983). The centrifugal horizontal cells in the lobula plate of the blowfly, Phaenicia sericata. J. Insect Physiol. *29*, 547-560.

Egelhaaf, M., and Borst, A. (1993). Motion computation and visual orientation in flies. Comp. Biochem. Physiol. *104*, 659–673.

Eichner, H., Joesch, M., Schnell, B., Reiff, D.F., and Borst, A. (2011). Internal structure of the fly elementary motion detector. Neuron *70*, 1155–1164.

Elyada, Y.M., Haag, J., and Borst, A. (2009). Different receptive fields in axons and dendrites underlie robust coding in motion-sensitive neurons. Nat. Neurosci. *12*, 327–332.

Farrow, K., Borst, A., and Haag, J. (2005). Sharing receptive fields with your neighbors: tuning the vertical system cells to wide field motion. J. Neurosci. *25*, 3985–3993.

Farrow, K., Haag, J., and Borst, A. (2006). Nonlinear, binocular interactions underlying flow field selectivity of a motion-sensitive neuron. Nat. Neurosci. *9*, 1312–1320.

Fischbach, P.K.F., and Dittrich, A.P.M. (1989). The optic lobe of *Drosophila melanogaster*. I. A Golgi analysis of wild-type structure. Cell Tissue Res. *258*, 441–475.

Fotowat, H., Fayyazuddin, A., Bellen, H.J., and Gabbiani, F. (2009). A novel neuronal pathway for visually guided escape in *Drosophila melanogaster*. J. Neurophysiol. *102*, 875–885.

Fry, S.N., Rohrseitz, N., Straw, A.D., and Dickinson, M.H. (2009). Visual control of flight speed in *Drosophila melanogaster*. J. Exp. Biol. *212*, 1120–1130.

Gauck, V., Egelhaaf, M., and Borst, A. (1997). Synapse distribution on VCH, an inhibitory, motion-sensitive interneuron in the fly visual system. J. Comp. Neurol. *381*, 489–499.

Georgopoulos, A.P., Schwartz, A.B., and Kettner, R.E. (1986). Neuronal population coding of movement direction. Science *233*, 1416–1419.

Grewe, J., Kretzberg, J., Warzecha, A.-K., and Egelhaaf, M. (2003). Impact of photon noise on the reliability of a motion-sensitive neuron in the fly's visual system. J. Neurosci. *23*, 10776–10783.

Grewe, J., Matos, N., Egelhaaf, M., and Warzecha, A.-K. (2006). Implications of functionally different synaptic inputs for neuronal gain and computational properties of fly visual interneurons. J. Neurophysiol. *96*, 1838–1847.

Haag, J., and Borst, A. (1997). Encoding of visual motion information and reliability in spiking and graded potential neurons. J. Neurosci. *17*, 4809–4819.

Haag, J., and Borst, A. (2001). Recurrent network interactions underlying flow-field selectivity of visual interneurons. J. Neurosci. *21*, 5685–5692.

Haag, J., and Borst, A. (2003). Orientation tuning of motion-sensitive neurons shaped by vertical-horizontal network interactions. J. Comp. Physiol. A *189*, 363–370.

Haag, J., Theunissen, F., and Borst, A. (1997). The intrinsic electrophysiological characteristics of fly lobula plate tangential cells: II. Active membrane properties. J Comput Neurosci *4*, 349–369.

Haag, J., Vermeulen, A., and Borst, A. (1999). The intrinsic electrophysiological characteristics of fly lobula plate tangential cells: III. Visual response properties. J Comput Neurosci *7*, 213–234.

Haag, J., and Borst, A. (2002). Dendro-dendritic interactions between motion-sensitive large-field neurons in the fly. J. Neurosci. *22*, 3227–3233.

Haag, J., and Borst, A. (2008). Electrical coupling of lobula plate tangential cells to a heterolateral motion-sensitive neuron in the fly. J. Neurosci. *28*, 14435–14442.

Haikala, V., Joesch, M., Borst, A., and Mauss, A.S. (2013). Optogenetic control of fly optomotor responses. J. Neurosci. *33*, 13927–13934.

"Robobees" http://robobees.seas.harvard.edu. (23/Dec./2014 available)

Hausen, K. (1982). Motion sensitive interneurons in the optomotor system of the fly. Biol. Cybernetics *45*, 143–156.

Heisenberg, M., Wonneberger, R., and Wolf, R. (1978). Optomotor-blind^{H31}—a *Drosophila* mutant of the lobula plate giant neurons. J. Comp. Physiol. *124*, 287–296.

Hodgkin, A.L., and Huxley, A.F. (1939). Action potentials recorded from inside a nerve fibre. Nature *144*, 710–711.

Horstmann, W., Egelhaaf, M., and Warzecha, A.-K. (2000). Synaptic interactions increase optic flow specificity. Eur. J. Neurosci. *12*, 2157–2165.

Hubel, D.H., and Wiesel, T.N. (1970). Stereoscopic vision in macaque monkey: Cells sensitive to binocular depth in area 18 of the macaque monkey cortex. Nature *225*, 41–42.

Huston, S.J., and Jayaraman, V. (2011). Studying sensorimotor integration in insects. Curr. Opin. Neurobiol. *21*, 527–534.

Ibbotson, M.R. (1991). Wide-field motion-sensitive neurons tuned to horizontal movement in the honeybee, Apis mellifera. J. Comp. Physiol. *168*, 91-102

Ito, M., Masuda, N., Shinomiya, K., Endo, K., and Ito, K. (2013). Systematic analysis of neural projections reveals clonal composition of the *Drosophila* brain. Curr. Biol. *23*, 1-12.

Joesch, M., Plett, J., Borst, A., and Reiff, D.F. (2008). Response properties of motion-sensitive visual interneurons in the lobula plate of *Drosophila melanogaster*. Curr. Biol. *18*, 368–374.

Joesch, M., Schnell, B., Raghu, S.V., Reiff, D.F., and Borst, A. (2010). ON and OFF pathways in *Drosophila* motion vision. Nature *468*, 300–304.

Joesch, M., Weber, F., Eichner, H., and Borst, A. (2013). Functional specialization of parallel motion detection circuits in the fly. J. Neurosci. *33*, 902–905.

Jolliffe, I. (2005). Principal Component Analysis (John Wiley & Sons, Ltd).

Jones, F.R.H. (1963). The reaction of fish to moving backgrounds. J. Exp. Biol. *40*, 437–446.

Juusola, M., and Hardie, R.C. (2001). Light adaptation in *Drosophila* photoreceptors: I. Response dynamics and signaling efficiency at 25°C. J. Gen. Physiol. *117*, 3–25.

Juusola, M., French, A.S., Uusitalo, R.O., and Weckström, M. (1996). Information processing by graded-potential transmission through tonically active synapses. Trends Neurosci. *19*, 292–297.

Kern, R., and Varjú, D. (1998). Visual position stabilization in the hummingbird hawk moth, *Macroglossum stellatarum L.* I. Behavioural analysis. J. Comp. Physiol. *182*, 225-237.

Kern, R., Nalbach, H.O., and Varjú, D. (1993). Interactions of local movement detectors enhance the detection of rotation. Optokinetic experiments with the rock crab, *Pachygrapsus marmoratus*. Vis. Neurosci. *10*, 643–652.

Kikuchi, A., Ohashi, S., Fuse, N., Ohta, T., Suzuki, M., Suzuki, Y., Fujita, T., Miyamoto, T., Aonishi, T., Miyakawa, H., et al. (2013). Experience-dependent

plasticity of the optomotor response in *Drosophila melanogaster*. Dev. Neurosci. *34*, 533–542.

Kimmerle, B., Egelhaaf, M., and Srinivasan, M.V. (1996). Object detection by relative motion in freely flying flies. Naturwissenschaften *83*, 380–381.

Kirchner, W.H., and Srinivasan, M.V. (1989). Freely flying honeybees use image motion to estimate object distance. Naturwissenschaften *76*, 281–282.

Krapp, H.G. (2009). Sensory integration: neuronal adaptations for robust visual self-motion estimation. Curr. Biol. *19*, R413–R416.

Krapp, H.G., Hengstenberg, R., and Egelhaaf, M. (2001). Binocular contributions to optic flow processing in the fly visual system. J. Neurophysiol. *85*, 724–734.

Kuramoto, Y. (2003). Chemical oscillations, waves, and turbulence (Springer).

Kurtz, R., Warzecha, A.K., and Egelhaaf, M. (2001). Transfer of visual motion information via graded synapses operates linearly in the natural activity range. J. Neurosci. *21*, 6957–6966.

Lemus, L., Hernández, A., Luna, R., Zainos, A., Nácher, V., and Romo, R. (2007). Neural correlates of a postponed decision report. Proc. Natl. Acad. Sci. U.S.A. *104*, 17174–17179.

Liu, G., Seiler, H., Wen, A., Zars, T., Ito, K., Wolf, R., Heisenberg, M., and Liu, L. (2006). Distinct memory traces for two visual features in the *Drosophila* brain. Nature *439*, 551–556.

Maimon, G., Straw, A.D., and Dickinson, M.H. (2010). Active flight increases the gain of visual motion processing in *Drosophila*. Nat. Neurosci. *13*, 393–399.

Maisak, M.S., Haag, J., Ammer, G., Serbe, E., Meier, M., Leonhardt, A., Schilling, T., Bahl, A., Rubin, G.M., Nern, A., et al. (2013). A directional tuning map of *Drosophila* elementary motion detectors. Nature *500*, 212–216.

Moeckel, R., and Liu, S.-C. (2007). Motion detection circuits for a Time-To-Travel algorithm. Circuits and Systems IEEE International Symposium, 3079-3082.

Moeckel, R., and Liu, S.-C. (2010). Motion detection chips for robotic platforms. Flying Insects and Robots. Chapter 8, 101-114. (Springer)

Morris, C., and Lecar, H. (1981). Voltage oscillations in the barnacle giant muscle fiber. Biophys. J. *35*, 193–213.

Muijres, F.T., Elzinga, M.J., Melis, J.M., and Dickinson, M.H. (2014). Flies evade looming targets by executing rapid visually directed banked turns. Science *344*, 172–177.

Neuser, K., Triphan, T., Mronz, M., Poeck, B., and Strauss, R. (2008). Analysis of a spatial orientation memory in *Drosophila*. Nature *453*, 1244–1247.

Newsome, W.T., Britten, K.H., and Movshon, J.A. (1989). Neuronal correlates of a perceptual decision. Nature *341*, 52–54.

Ofstad, T.A., Zuker, C.S., and Reiser, M.B. (2011). Visual place learning in *Drosophila melanogaster*. Nature *474*, 204–207.

Rauschecker, J.P., Grünau, von, M.W., and Poulin, C. (1987). Centrifugal organization of direction preferences in the cat's lateral suprasylvian visual cortex and its relation to flow field processing. J. Neurosci. *7*, 943–958.

Reichardt, W. (1987). Evaluation of optical motion information by movement detectors. J. Comp. Physiol. *161*, 533–547.

Reichardt, W., Poggio, T., and Hausen, K. (1983). Figure-ground discrimination by relative movement in the visual system of the fly. Biol. Cybernetics *46*, 1–30.

Reichel, L., Liechti, D., Presser, K., and Liu, S. C. (2005). Range estimation on a robot using neuromorphic motion sensors. Robotics and Autonomous Systems *51*, 167–174.

Reiser, M.B., and Dickinson, M.H. (2008). A modular display system for insect behavioral neuroscience. J. Neurosci. Methods *167*, 127–139.

Reyn, von, C.R., Breads, P., Peek, M.Y., Zheng, G.Z., Williamson, W.R., Yee, A.L., Leonardo, A., and Card, G.M. (2014). A spike-timing mechanism for action selection. Nat. Neurosci. *17*, 962-970.

Sanes, J.R., and Zipursky, S.L. (2010). Design principles of insect and vertebrate visual systems. Neuron *66*, 15–36.

Sasaki, T., Matsuki, N., and Ikegaya, Y. (2007). Metastability of active CA3 networks. J. Neurosci. *27*, 517–528.

Schlotterer, G.R. (1977). Response of the locust descending movement detector neuron to rapidly approaching and withdrawing visual stimuli. Canadian J. Zoology. *55*, 1372–1376.

Schnell, B., Joesch, M., Forstner, F., Raghu, S.V., Otsuna, H., Ito, K., Borst, A., and Reiff, D.F. (2010). Processing of horizontal optic flow in three visual interneurons of the *Drosophila brain*. J. Neurophysiol. *103*, 1646–1657.

Schnell, B., Weir, P.T., Roth, E., Fairhall, A.L., and Dickinson, M.H. (2014). Cellular mechanisms for integral feedback in visually guided behavior. Proc. Natl. Acad. Sci. U.S.A. *111*, 5700–5705.

Seelig, J.D., Chiappe, M.E., Lott, G.K., Dutta, A., Osborne, J.E., Reiser, M.B., and Jayaraman, V. (2010). Two-photon calcium imaging from head-fixed *Drosophila* during optomotor walking behavior. Nat. Methods *7*, 535–540.

"Green Brain Project" http://greenbrain.group.shef.ac.uk. (23/Dec./2014 available)

Srinivasan, M., Zhang, S., Lehrer, M., and Collett, T. (1996). Honeybee navigation en route to the goal: visual flight control and odometry. J. Exp. Biol. *199*, 237–244.

Stopfer, M., Jayaraman, V., and Laurent, G. (2003). Intensity versus identity coding in an olfactory system. Neuron *39*, 991–1004.

Suzuki, Y., Morimoto, T., Miyakawa, H., and Aonishi, T. (2014). Cooperative integration and representation underlying bilateral network of fly motion-sensitive neurons. PLoS ONE *9*, e85790.

Tanaka, K., and Saito, H. (1989). Analysis of motion of the visual field by direction, expansion/contraction, and rotation cells clustered in the dorsal part of the medial superior temporal area of the macaque monkey. J. Neurophysiol. *62*, 626–641.

Tang, S. (2001). Choice behavior of *Drosophila* facing contradictory visual cues. Science *294*, 1543–1547.

Torben-Nielsen, B., and Stiefel, K.M. (2010). Wide-field motion integration in fly VS cells: insights from an inverse approach. PLoS Comput. Biol. *6*, e1000932.

van Swinderen, B. (2007). Attention-like processes in *Drosophila* require short-term memory genes. Science *315*, 1590–1593.

van Swinderen, B., and Flores, K.A. (2007). Attention-like processes underlying optomotor performance in a *Drosophila* choice maze. Dev Neurobiol *67*, 129–145.

van Swinderen, B., McCartney, A., Kauffman, S., Flores, K., Agrawal, K., Wagner, J., and Paulk, A. (2009). Shared visual attention and memory systems in the *Drosophila* brain. PLoS ONE *4*, e5989.

Verghese, P., Watamaniuk, S.N., McKee, S.P., and Grzywacz, N.M. (1999). Local motion detectors cannot account for the detectability of an extended trajectory in noise. Vision Research *39*, 19–30.

Vogt, K., Schnaitmann, C., Dylla, K.V., Knapek, S., Aso, Y., Rubin, G.M., and Tanimoto, H. (2014). Shared mushroom body circuits underlie visual and olfactory memories in *Drosophila*. Elife *3*, e02395.

Waddell, S., and Quinn, W.G. (2001). What can we teach *Drosophila*? What can they teach us? Trends Genet. *17*, 719–726.

Warrant, E.J. (1999). Seeing better at night: life style, eye design and the optimum strategy of spatial and temporal summation. Vision Research *39*, 1611–1630.

Warrant, E. (2004). Vision in the dimmest habitats on earth. J. Comp. Physiol. A *190*, 765–789.

Watamaniuk, S.N., McKee, S.P., and Grzywacz, N.M. (1995). Detecting a trajectory embedded in random-direction motion noise. Vision Research *35*, 65–77.

Wylie, D.R., and Frost, B.J. (1990). Binocular neurons in the nucleus of the basal optic root (nBOR) of the pigeon are selective for either translational or rotational visual flow. Vis. Neurosci. *5*, 489–495.

Yaksi, E., and Wilson, R.I. (2010). Electrical coupling between olfactory glomeruli. Neuron *67*, 1034–1047.

Zhang, K., Guo, J.Z., Peng, Y., Xi, W., and Guo, A. (2007). Dopamine-mushroom body circuit regulates saliency-based decision-making in *Drosophila*. Science *316*, 1901–1904.

Zhu, Y., Nern, A., Zipursky, S.L., and Frye, M.A. (2009). Peripheral visual circuits functionally segregate motion and phototaxis behaviors in the fly. Curr. Biol. *19*, 613–619.

Figures

Figure 1 Behavioral experiment in a tethered fly.

(a) Schematic diagram of the apparatus. A fly is fixed to a steel pin and placed in the center of an LED arena that displays visual stimuli controlled by a PC. Head movements are recorded on a CCD camera above the arena to measure the OMR. (b) When presented with a yaw rotation motion stimulus, a fly rotates its head to follow the motion (top). The head yawing angles can be computed from videos recorded by the camera. Examples of two individual traces of the head yaw response during CW and CCW motion (bottom). The original position is not always centered because flies move their heads freely before stimulus presentation. (c) Visual stimuli are constructed by the superimposition of random dot noise independently added from frame to frame on a panoramic vertically striped square-wave grating. When a 'random dot' LED was placed on a bright bar of the original stripe pattern, the intensity of the random dot was subtracted from the bright bar. Thus, the total LED display intensity was kept constant in each frame. The temporal sequence of an individual trial is shown (bottom).

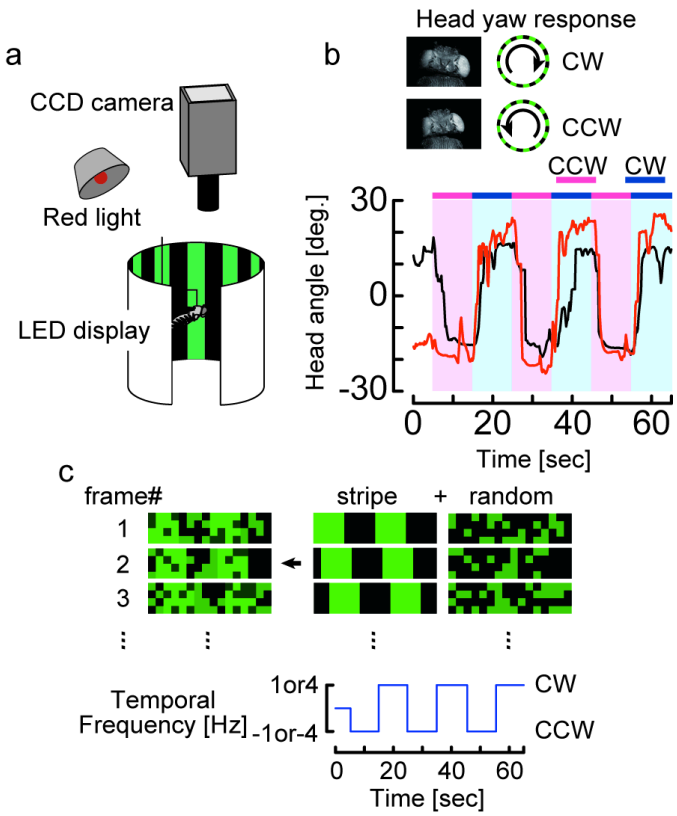
a
CCD camera
Red light
LED display
b
Head yaw response
CW
CCW
CCW
CW
Head angle [deg.]
30
0
-30
0
20
40
60
Time [sec]
c
frame#
1
2
3
stripe
+
random
Temporal
Frequency [Hz]
1or4
-1or-4
CW
CCW
0
20
40
60
Time [sec]

Figure 2 Flies can robustly discriminate wide-field motion directions under noisy conditions.

(a) Average of head yaw responses ± s.e.m. (upper panels) and distributions of head angle (lower panels) shown over a range of SNR at 1 and 4 Hz temporal frequencies. Stimulus patterns and SNR are as depicted above each figure. Stripe denotes the stripe pattern without noise. (red, CCW rotation; blue, CW rotation; n = 20 flies, 36 trials at 1 Hz temporal frequency; n = 9 flies, 17 trials at 4 Hz). (b) ROCs for the six pairs of CCW-CW response distributions illustrated in a. Increased separation of CCW and CW response distributions in a leads to an increased deflection of the ROC away from the diagonal. (c) Area under the ROC curves (AUC) illustrated in b. When the ROC curve lies along the diagonal, which indicates that the fly cannot distinguish between CCW and CW rotations, the AUC is 0.5. When the ROC curve approaches the left axis and upper limit, which indicates that fly fully distinguishes between CCW and CW, the AUC is 1.0.

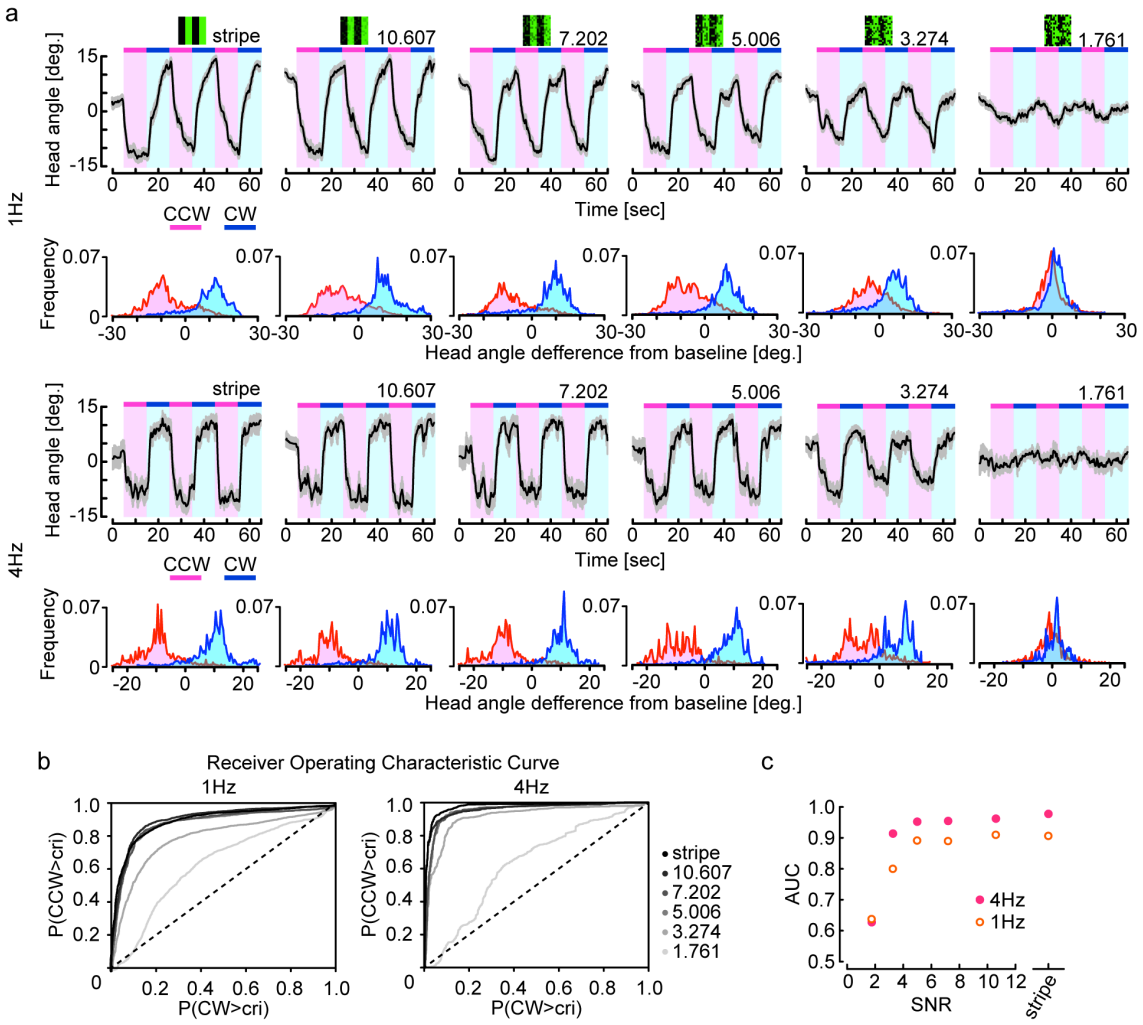
a
1Hz
4Hz
stripe
10.607
7.202
5.006
3.274
1.761
Head angle [deg.]
Time [sec]
CCW
CW
Frequency
Head angle defference from baseline [deg.]
b
Receiver Operating Characteristic Curve
1Hz
4Hz
P(CCW>cri)
P(CW>cri)
stripe
10.607
7.202
5.006
3.274
1.761
c
AUC
SNR
4Hz
1Hz

Figure 3 Strong correlation between the discriminative capacity of the OMR and HS cells to motion stimuli with noise.
(a) Schematic diagram of the recording apparatus. (b) A recorded biocytin-filled HS cell (green) located in the right hemisphere (posterior view). Scale bar = 100 m m. OL, optic lobe (c) A space-time plot of the rotation stimuli. Each bar is 15 ° in azimuthal extent, and the temporal frequency is 1 Hz. (d) Example of response of a single right HS cell to a stripe pattern moving PD (CW) or ND (CCW) at a temporal frequency of 1 Hz. The gray-shaded region indicates the period when visual stimuli were in motion (1 s). HS cell are depolarized or hyperpolarized during PD or ND, respectively. (e) Average membrane potentials ± s.e.m. of an HS cell to visual stimuli of different SNR moving in PD and ND (top panel). The bottom panel shows the distributions of baseline-subtracted membrane potentials during stimulus presentation (red, ND; blue, PD). We noted that HS cells also depolarized during ND motion stimulation even when the SNR of the stimulus is at a low level. This is speculated to be due to random dot blinking because the random dot pattern becomes a dominant component in the visual pattern at low SNR levels. (f) ROCs for the five pairs of PD-ND response distributions illustrated in e. (g) Mean ± s.e.m. of AUC (red, HS cell, n = 10 cells; gray, behavior). The same behavioral data from Figure 2c (at 1 Hz) is also presented. (h) Mean ± s.e.m. of baseline-subtracted responses to PD and ND directions over a range of SNR. Responses of individual cells were calculated by integrating baseline-subtracted mean membrane potentials over the trials during motion presentation. (n = 10 cells) (i) Mean ± s.e.m. of difference between the PD and ND responses illustrated in h (MRD, mean response difference).

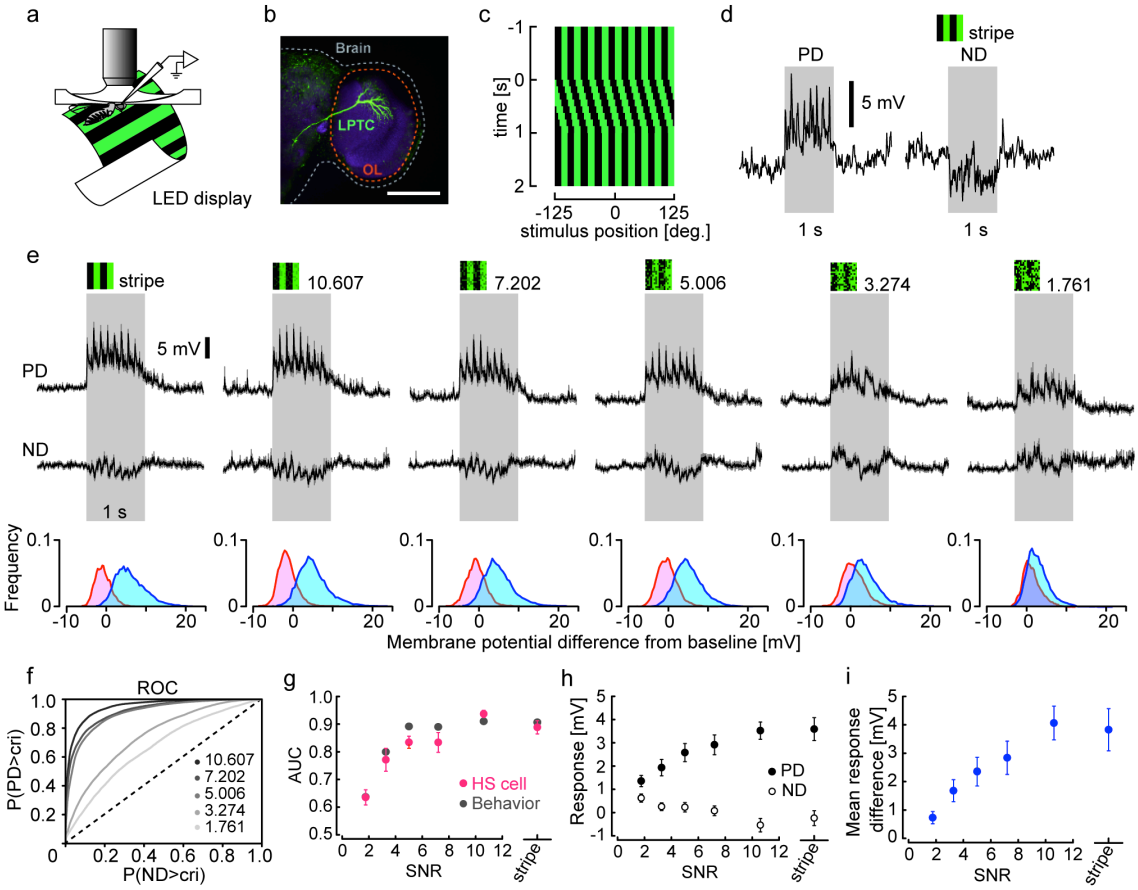
a
LED display
b
Brain
LPTC
OL
c
time [s]
stimulus position [deg.]
d
stripe
PD
ND
5 mV
1 s
e
stripe
10.607
7.202
5.006
3.274
1.761
PD
ND
5 mV
1 s
Frequency
Membrane potential difference from baseline [mV]
f
ROC
P(PD>cri)
P(ND>cri)
g
AUC
SNR
HS cell
Behavior
h
Response [mV]
SNR
PD
ND
i
Mean response difference [mV]
SNR

Figure 4 Unilateral visual input is sufficient to generate the features of HS activities in response to motion stimuli with noise. (a) Schematic diagram of the experimental condition. One side of fly's compound eyes was covered with an aluminum foil barrier to block visual inputs from the contralateral side of the recorded HS cell. (b) Average membrane potentials of 6 cells (red, covered) and 10 cells (black, uncovered) that responded to visual stimuli with different SNR moving in PD and ND at a temporal frequency of 1 Hz. The gray-shaded region indicates when the visual stimulus was in motion. (c) Mean ± s.e.m. of AUC (red, covered, n = 6 cells; gray, uncovered cell data from Figure 3g; $p > 0.05$, two-way ANOVA) (d) Mean ± s.e.m. of baseline-subtracted responses to PD or ND motion obtained from covered HS cells at different SNR. Responses of an individual cell were calculated by baseline-subtracted mean membrane potentials over trials integrated during motion (n = 6 cells). (e) Mean ± s.e.m. of MRD (blue, covered; gray, uncovered. The uncovered data are the same as in Figure 3i ($p > 0.05$, two-way ANOVA).

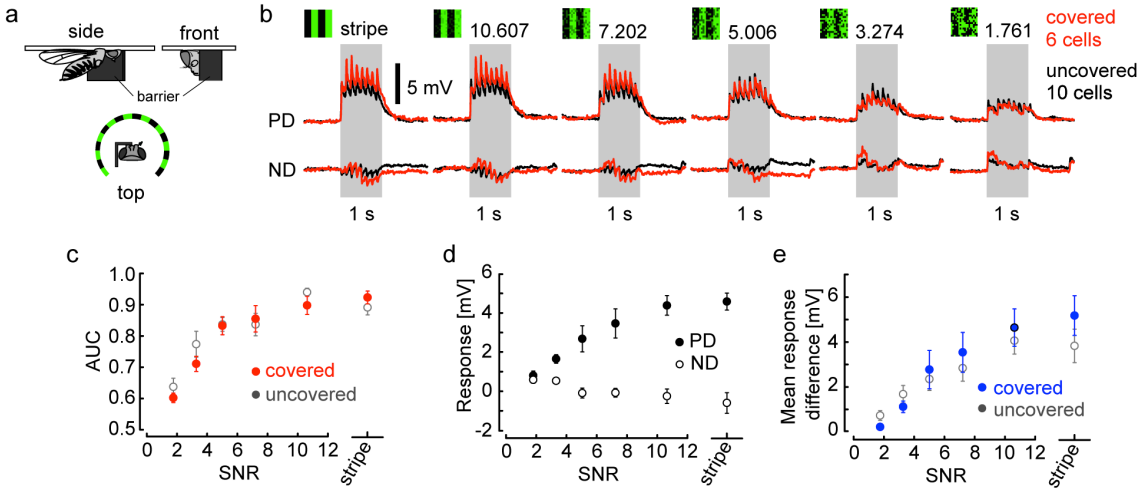
a
side
front
barrier
top
b
stripe
10.607
7.202
5.006
3.274
1.761
covered
6 cells
uncovered
10 cells
5 mV
PD
ND
1 s
c
AUC
covered
uncovered
SNR
stripe
d
Response [mV]
PD
ND
SNR
stripe
e
Mean response difference [mV]
covered
uncovered
SNR
stripe

Figure 5 An EMD model that adds a spatial filter and threshold function reproduces the experimental results.

(a) The structure of our model. First, the visual stimulus is filtered with a 2D Gaussian function (σ = 7.5°), and the filtered signal is passed through a sigmoid function (threshold function). The sigmoidal output is processed by the 2D array of a 2-Quadrant-Detector model (see Methods). HP, temporal first-order high-pass filter (τ = 250 ms); DC, passing 10% of the original signal; LP, temporal first-order low-pass filter (τ = 150 ms); M, multiplication; Sigma (Σ), nonlinear integration. (b) Putative 2D appearance of the LED display from the tethered fly (top). The spatial distribution of dendritic integration for the model cells (bottom). We constructed the vector field of spatial weight factors $[w_h, w_v]$ adjusted for the receptive field of the right HS cell (Krapp et al., 2001). The length and orientation of each vector indicates the level of sensitivity and the preferred direction of local motion detector, respectively. (c) Average responses of the model cell (10 trials) to visual stimuli with various SNR in both PD and ND stimulations at a temporal frequency of 1 Hz. The gray-shaded region indicates when visual stimuli were in motion. (d) Mean AUC (red, contained both the spatial filter and threshold function as illustrated in a; gray, contained either the spatial filter or threshold function). (e) Mean normalized response difference (normalized MRD) between PD and ND motion stimulus for each model (10 trials). MRDs were normalized by the response to the stripe motion stimulus for each condition (blue, contained both the spatial filter and threshold function [filled circles] and HS cells calculated from the in Figure 3i [open circles]; gray, contained either the spatial filter or threshold function).

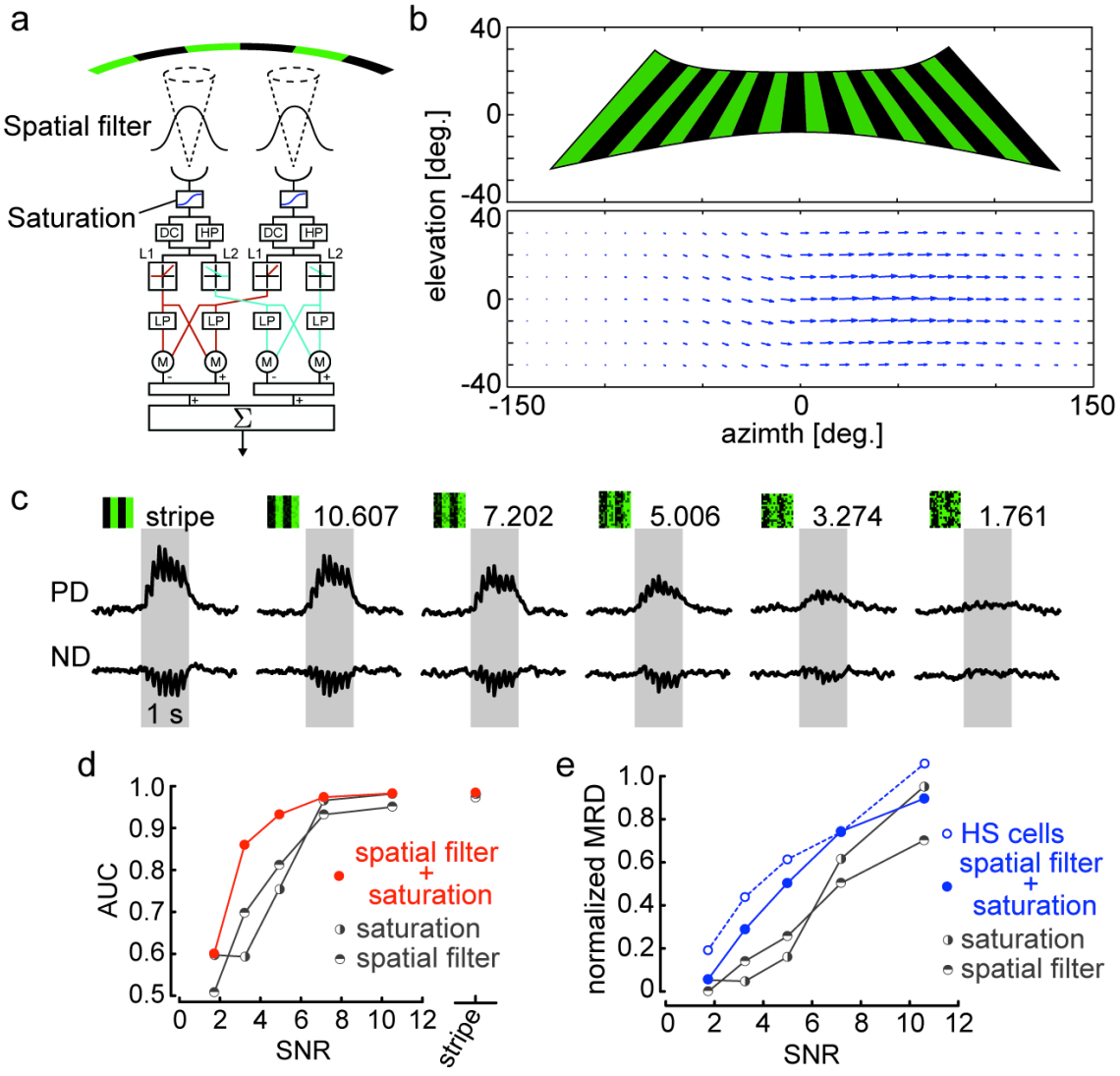
a
Spatial filter
Saturation
DC
HP
L1
L2
LP
M
Σ
b
40
0
-40
elevation [deg.]
-150
0
150
azimth [deg.]
c
stripe
10.607
7.202
5.006
3.274
1.761
PD
ND
1 s
d
AUC
1.0
0.9
0.8
0.7
0.6
0.5
0
2
4
6
8
10
12
SNR
stripe
spatial filter + saturation
saturation
spatial filter
e
normalized MRD
1.0
0.8
0.6
0.4
0.2
0
SNR
HS cells
spatial filter + saturation
saturation
spatial filter

Figure 6 Schematic diagrams of the fly optic lobe and circuit of LPTCs with horizontal preferred directions.

A: Fly visual system consisting of neuropils called the lamina, medulla, and lobula complex in the two hemispheres. Visual motion information on each side of the visual field is retinotopically processed through the lamina and medulla and converges on the lobula complex in the ipsilateral hemisphere. The complex contains a set of wide-field motion-sensitive neurons, called lobula plate tangential cells (LPTCs). B: Bilateral network of the LPTCs with horizontal preferred directions. Each hemisphere consists of eight cells: those named Hu, H1 and H2 are spiking neurons (colored), whereas the others named HS and CH are graded-potential neurons (gray). These LPTCs are mutually coupled through intrahemispheric and interhemispheric connections. Open triangles, bars and resister symbols indicate excitatory, inhibitory and electrical synapses, respectively. The cells with black arrows receive projections from the first-order neuropils, and the direction of each arrow denotes the preferred direction of each cell. dCH and vCH (without black arrows) do not directly receive projections from the first-order neuropils.

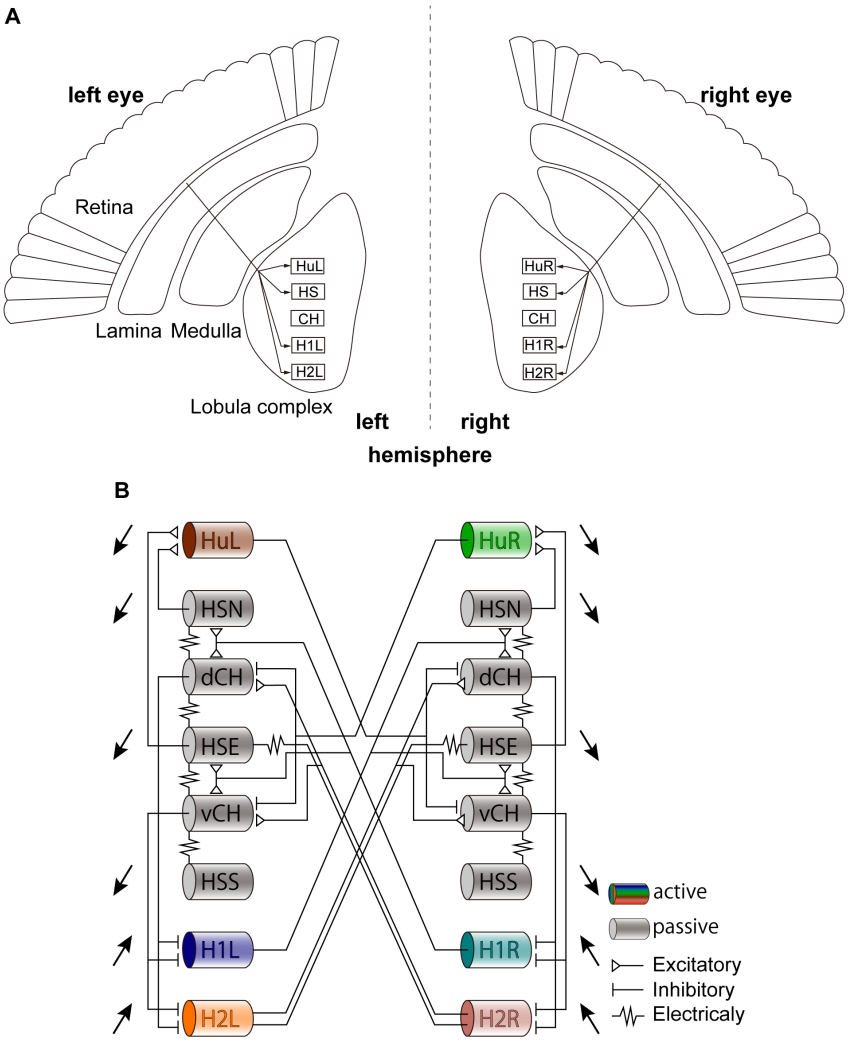
A
left eye
right eye
Retina
Lamina
Medulla
Lobula complex
HuL
HS
CH
H1L
H2L
HuR
HS
CH
H1R
H2R
left
hemisphere
right
B
HuL
HSN
dCH
HSE
vCH
HSS
H1L
H2L
HuR
HSN
dCH
HSE
vCH
HSS
H1R
H2R
active
passive
Excitatory
Inhibitory
Electricaly

Figure 7 Activities of the H2 cell strongly depend on interhemispheric couplings between H2 and contralateral HSE. Gray in all figures: Responses of the H2L cell to the ipsilateral PD motion stimulus in the disconnected case. Red and blue: Responses of the H2L cell to the clockwise and back-to-front motion stimuli in the connected case (A, B and C) and the case without the interhemispheric electrical couplings (D and E). A: Raster plots showing locations of action potentials of the H2L cell in time for a single trial (SNR = 0.166). B: Differences in mean firing rate from spontaneous activity in the H2L cell in response to these motion stimuli with different noise levels. The abscissa indicates the signal-to-noise ratio of motion stimuli. The ordinate indicates difference between firing rates during stimulations and spontaneous activity. (Mean ± s.e.m., 8 trials) C: ISI distributions of the H2L cell in response to PD motion stimuli (SNR=0.166). D: Differences in mean firing rates of the H2L cell without the interhemispheric electrical couplings. (Mean ± s.e.m., 8 trials) E: ISI distributions of the H2L cell without the electrical couplings. (SNR = 0.166). As shown in B and C, although the H2L cell directly faces the PD motion stimuli in the clockwise and back-to-front cases, the activity and regularity of the H2L cell for the clockwise motion stimulus are higher than those of the back-to-front stimulus because of the modification by contralateral LPTC activities. If the interhemispheric electrical couplings are only cut off and other connections remain in the bilateral network, as revealed in D and E, the activity and regularity of the H2L cell in this case is almost same as that in the disconnected case. Thus, these results suggest that the interhemispheric electrical couplings are a key factor to determining the responsive characteristics of the H2 cell to the binocular motion stimuli.

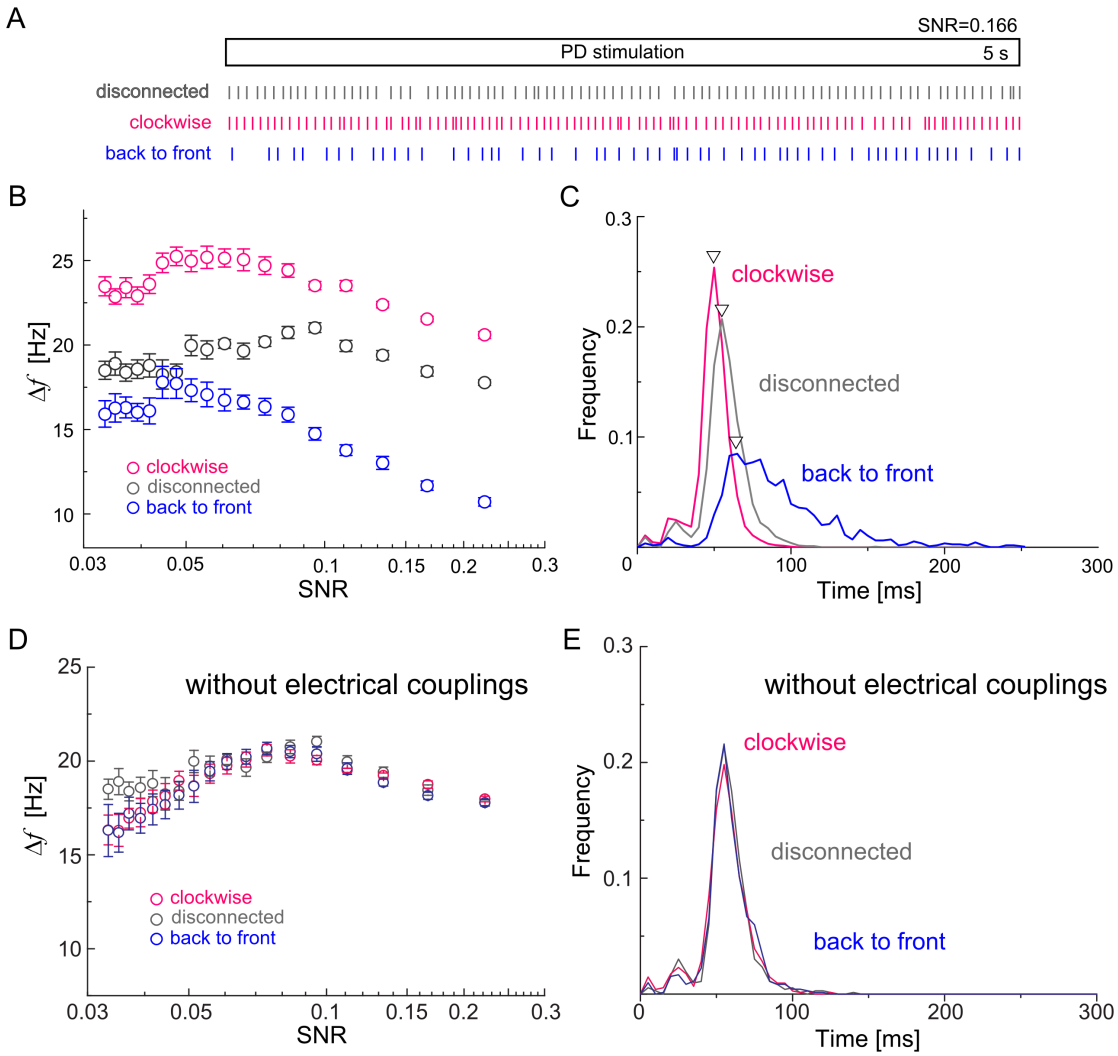
A
SNR=0.166
PD stimulation
5 s
disconnected
clockwise
back to front
B
Δf [Hz]
SNR
clockwise
disconnected
back to front
C
Frequency
Time [ms]
clockwise
disconnected
back to front
D
without electrical couplings
Δf [Hz]
SNR
clockwise
disconnected
back to front
E
without electrical couplings
Frequency
Time [ms]
clockwise
disconnected
back to front

Figure 8 Change in firing-rate correlations between two spiking LPTCs depending on binocular stimuli.

Left column: In- phase motion stimulus (clockwise). Right column: Out-of-phase motion stimulus (back-to-front). A and B: Cross-correlations between the H1 and H2 cells located in the left hemisphere. C: Cross-correlation between the H1 and Hu cells separately located in two hemispheres. D: Cross-correlation between two H1 cells separately located in two hemispheres. Note that the two LPTCs in each pair shown in these graphs receive PD motion stimuli in the in-phase and out-of-phase cases, respectively. The peak of the cross-correlations of the H1 and H2 cells at a lag of 0 sec for the in-phase motion stimulus is higher than that of the out-of-phase motion stimulus. Whereas the responsiveness of single H1 and Hu cells does not change with the contralateral motion stimuli (Figure 9 and 10), the peak of the cross-correlations of these for the in-phase motion stimulus is higher than that of the out-of- phase motion stimulus.

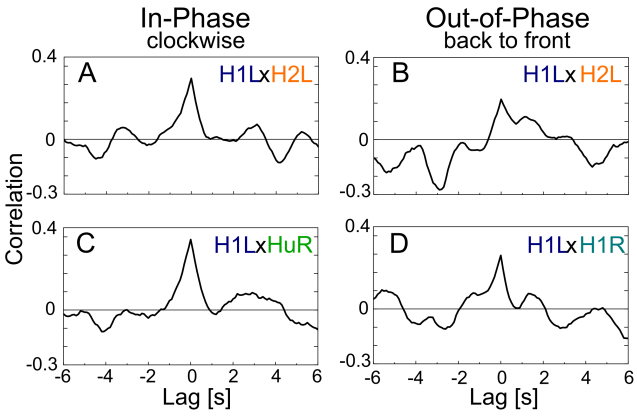
In-Phase
clockwise
Out-of-Phase
back to front
A
H1LxH2L
B
H1Lx H2L
C
H1LxHuR
D
H1LxH1R
Correlation
0.4
0
-0.3
-6
-4
-2
0
2
4
6
Lag [s]

Figure 9 Activities of the H1L cell in response to PD motion stimuli are not modified by contralateral LPTC activities.
(gray) Responses of the H1L cell to the ipsilateral PD motion stimulus in the disconnected case. (red) Responses of the H1L cell to the clockwise motion stimulus in the connected case. (blue) Responses of the H1L cell to the back-to-front motion stimulus in the connected case. A: Differences in mean firing rate from spontaneous activity in the H1L cell in response to these motion stimuli with different noise levels. The abscissa is the signal-to- noise ratio of the motion stimuli. The ordinate is the difference between firing rates during stimulation and spontaneous activity. (Mean ± s.e.m., 8 trials) B: ISI distributions of the H1L cell in response to PD motion stimuli (SNR = 0.166). The activity and regularity of the H1L cell when the facing of the clockwise motion stimulus is almost the same as that of the back-to-front stimulus.

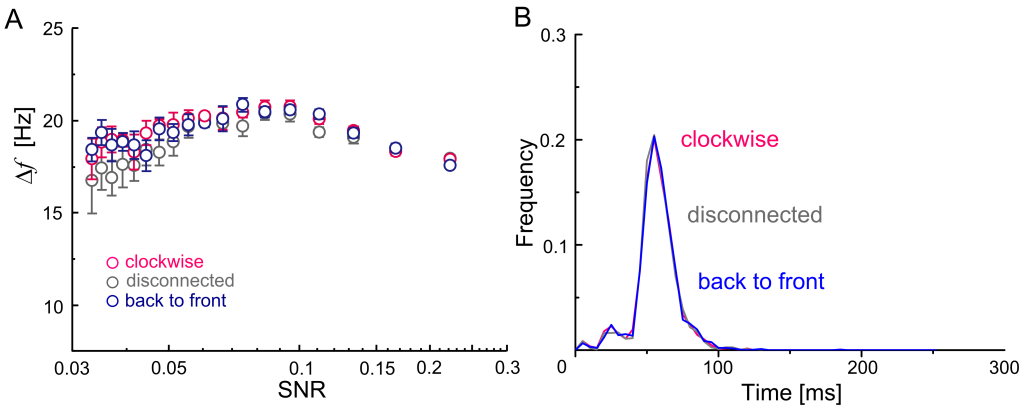
A
25
20
15
10
Δf [Hz]
clockwise
disconnected
back to front
0.03
0.05
0.1
0.15
0.2
0.3
SNR
B
0.3
0.2
0.1
0
Frequency
clockwise
disconnected
back to front
100
200
300
Time [ms]

Figure 10 Activities of the HuL cell in response to PD motion stimuli are not modified by contralateral LPTC activities.
(gray) Responses of the HuL cell to the ipsilateral PD motion stimulus in the disconnected case. (red) Responses of the HuL cell to the counterclockwise motion stimulus in the connected case. (blue) Responses of the HuL cell to the front-to-back motion stimulus in the connected case. A: Differences in mean firing rate from spontaneous activity in the HuL cell in response to stimuli with different noise levels. The abscissa indicates the signal-to-noise ratio of motion stimuli. The ordinate indicates differences between firing rates during stimulations and spontaneous ones. (Mean ± s.e.m., 8 trials) B: ISI distributions of the HuL cell in response to PD motion stimuli (SNR=0.166). The activity and regularity of the HuL cell when the facing of the counterclockwise motion stimulus is almost same as that of the front-to-back stimulus.

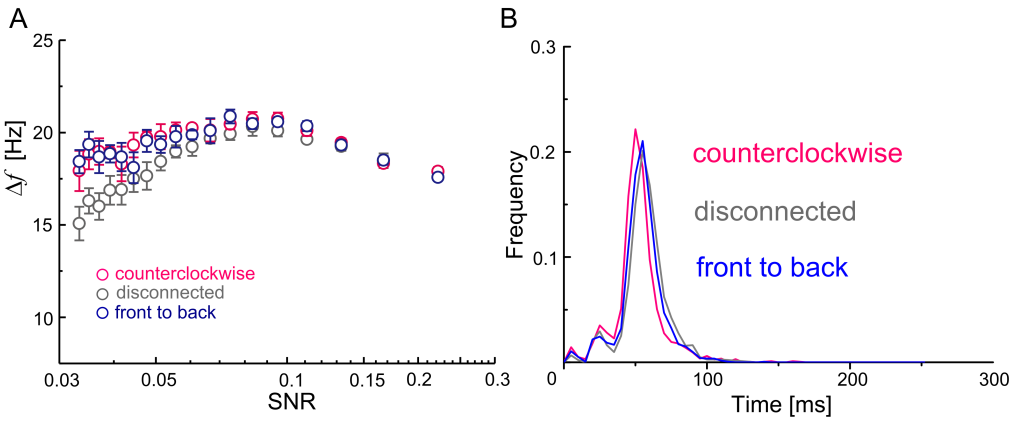
A
25
20
15
10
Δf [Hz]
0.03
0.05
0.1
0.15
0.2
0.3
SNR
counterclockwise
disconnected
front to back
B
0.3
0.2
0.1
0
Frequency
100
200
300
Time [ms]
counterclockwise
disconnected
front to back

Figure 11 Coding properties of a population of LPTCs in a bilateral network.

A: Raster plots showing locations of action potentials of all six spiking LPTCs in time for a single trial with the four different stimuli. Red plots indicate responses of spiking LPTCs in the connected case, and black plots present responses of spiking LPTCs in the disconnected case. B: Principal component analysis (PCA) for population activities shown in A. The firing rate vectors are projected onto a two-dimensional space spanned by the first and second principal components, PC1 and PC2. Colors indicate different stimuli. In the disconnected case, four clusters of the firing rate vectors corresponding to the four different stimuli are respectively separated into the four quadrants, whereas in the connected case, clusters of the firing rate vectors corresponding to the in-phase and out-of-phase stimuli are respectively distributed along the PC1 and PC2 axes. C: Contribution ratio of PC1 and PC2 (bars) and cumulative contribution ratio (dots) in the connected and disconnected cases. (Mean ± s.e.m., 10 trials).

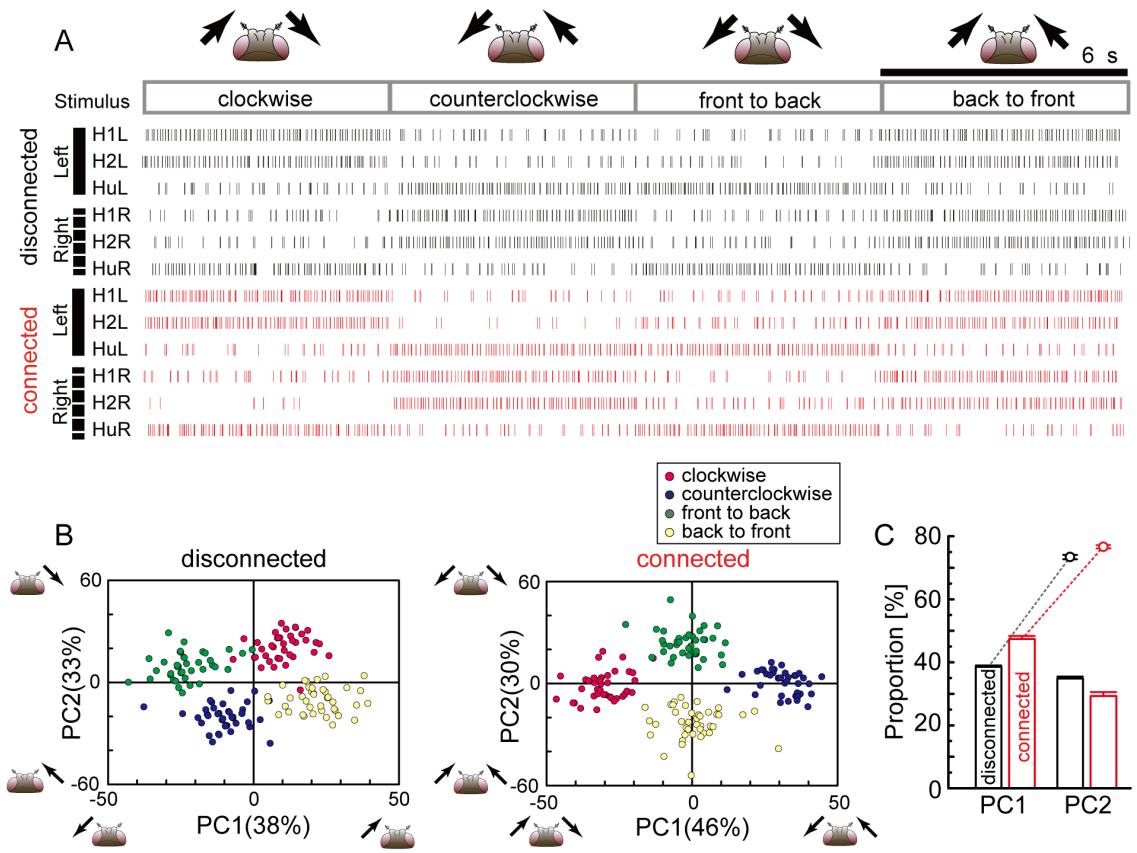
A
6 s
Stimulus
clockwise
counterclockwise
front to back
back to front
disconnected
connected
Left
Right
H1L
H2L
HuL
H1R
H2R
HuR
B
disconnected
connected
clockwise
counterclockwise
front to back
back to front
PC2(33%)
PC1(38%)
PC2(30%)
PC1(46%)
60
0
-60
-50
0
50
C
Proportion [%]
80
60
40
20
0
disconnected
connected
PC1
PC2

Figure 12 Each element of the first two principal components, PC1 and PC2, in five trials of numerical simulations for the detailed model with different random seeds for noise.

The upper table is the disconnected case, and the lower table is the connected case. What each principle component codes in the five trials is presented on the margins of these tables. In the connected case, PC1 and PC2 stably represent the in-phase and out-phase motions, whereas in the disconnected case, PC1 and PC2 are randomly assigned to either left or right monocular motion.

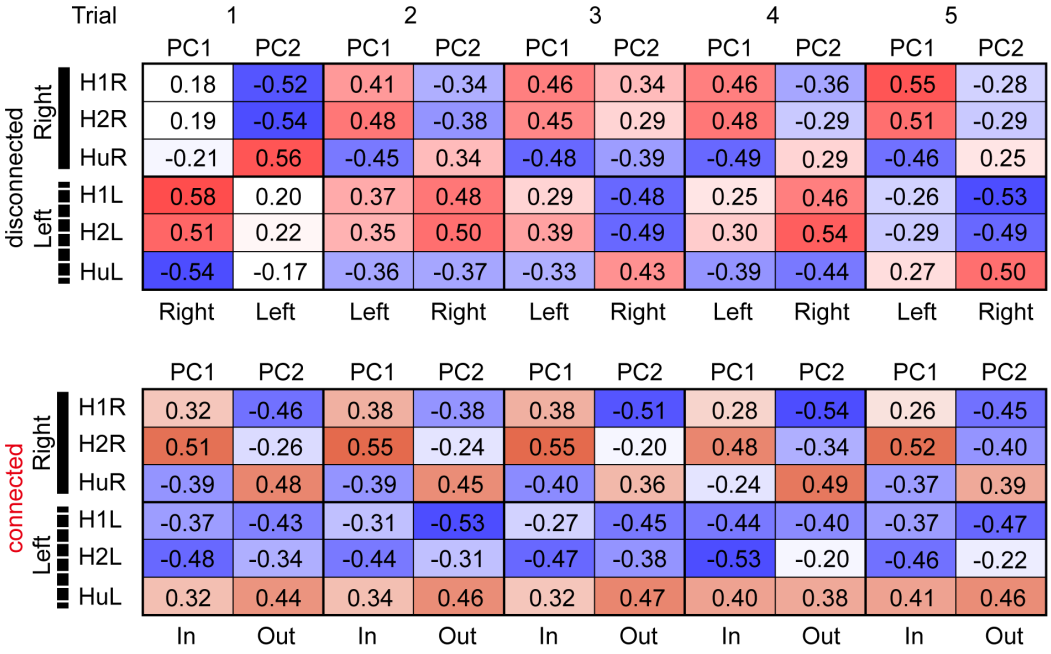
Trial
1
2
3
4
5
PC1
PC2
disconnected
Right
Left
H1R
H2R
HuR
H1L
H2L
HuL
0.18 -0.52 0.41 -0.34 0.46 0.34 0.46 -0.36 0.55 -0.28
0.19 -0.54 0.48 -0.38 0.45 0.29 0.48 -0.29 0.51 -0.29
-0.21 0.56 -0.45 0.34 -0.48 -0.39 -0.49 0.29 -0.46 0.25
0.58 0.20 0.37 0.48 0.29 -0.48 0.25 0.46 -0.26 -0.53
0.51 0.22 0.35 0.50 0.39 -0.49 0.30 0.54 -0.29 -0.49
-0.54 -0.17 -0.36 -0.37 -0.33 0.43 -0.39 -0.44 0.27 0.50
Right Left Left Right Left Right Left Right Left Right
connected
0.32 -0.46 0.38 -0.38 0.38 -0.51 0.28 -0.54 0.26 -0.45
0.51 -0.26 0.55 -0.24 0.55 -0.20 0.48 -0.34 0.52 -0.40
-0.39 0.48 -0.39 0.45 -0.40 0.36 -0.24 0.49 -0.37 0.39
-0.37 -0.43 -0.31 -0.53 -0.27 -0.45 -0.44 -0.40 -0.37 -0.47
-0.48 -0.34 -0.44 -0.31 -0.47 -0.38 -0.53 -0.20 -0.46 -0.22
0.32 0.44 0.34 0.46 0.32 0.47 0.40 0.38 0.41 0.46
In Out In Out In Out In Out In Out

Figure 13 The neuronal morphologies do not affect on the population coding properties.

A: Principal component analysis (PCA) for population activities. I analyzed population coding properties under conditions in which the length of each LPTC is two-third that of the original model. The firing rate vectors are projected onto a two-dimensional space spanned by the first and second principal components, PC1 and PC2. Colors indicate different stimuli. Clusters of the firing rate vectors corresponding to the in-phase and out-of-phase stimuli are respectively distributed along the PC1 and PC2 axes. This result is the qualitatively same as those shown in Figure 11B. B: Contribution ratio of PC1 and PC2 (bars) and cumulative contribution ratio (dots). (Mean ± s.e.m., 10 trials).

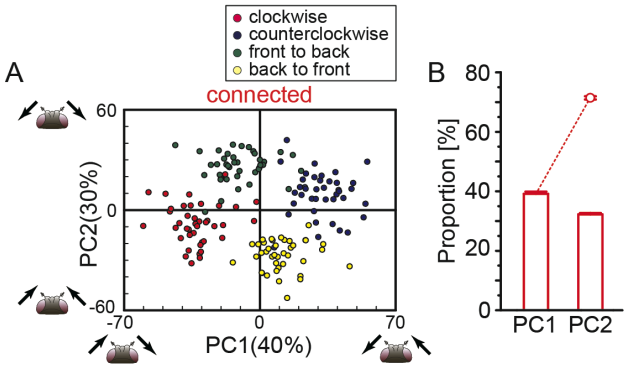
A
clockwise
counterclockwise
front to back
back to front
connected
60
0
-60
PC2(30%)
-70
0
70
PC1(40%)
B
80
60
40
20
0
Proportion [%]
PC1
PC2

Figure 14 Interhemispheric couplings between H2 and HSE cells mainly affect the coding properties of population activities.

A: PCAs for population activities using different values of the conductance of the electrical coupling. As in Figure 11B, the firing rate vectors are projected onto a two-dimensional space spanned by PC1 and PC2. Colors indicate different stimuli. B: Contribution ratio of PC1 and PC2 as a function of the conductance of the electrical coupling. For comparison, the contribution ratio in the disconnected case is superimposed on this graph. As the conductance of the electrical coupling increases, the difference between contribution rates of PC1 and PC2 becomes larger. In the disconnected case and the case with the electrical coupling of 0 nS, the differences are relatively small, and four clusters of population activities corresponding to the four different stimuli are separated into the four quadrants, as shown in Figs. 11A and 11B. (Mean ± s.e.m., 10 trials).

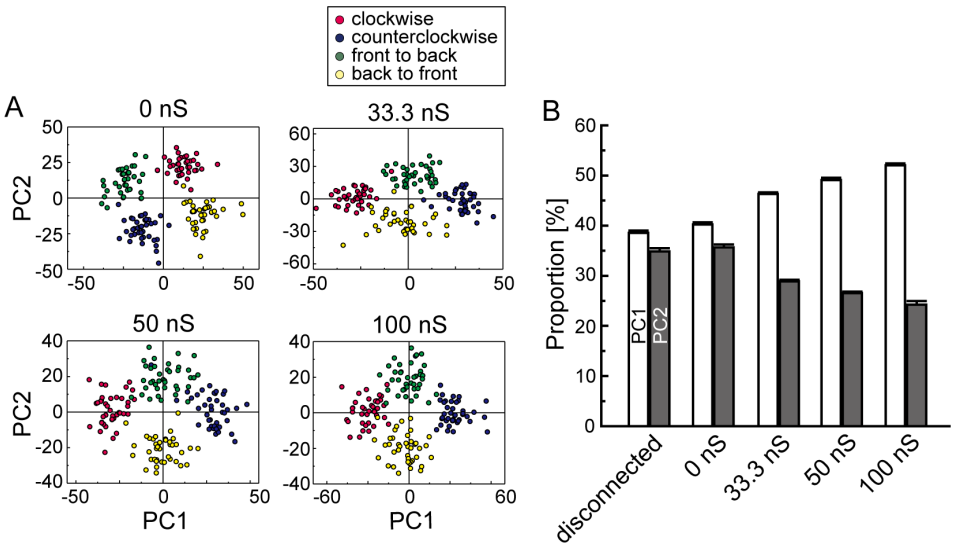
A
clockwise
counterclockwise
front to back
back to front
0 nS
33.3 nS
50 nS
100 nS
PC2
PC1
B
Proportion [%]
PC1
PC2
disconnected
0 nS
33.3 nS
50 nS
100 nS

Figure 15 Coding properties are conserved in the reduced model.
A: Summary diagram of the reduced model. For simplicity, in each hemisphere, five graded-potential cells are merged into a single cell named HS/CH. All cells are described using the McCulloch-Pitts model instead of the conductance-based model. B: Activities of three LPTCs corresponding to the spiking cells on the left side in response to the four different stimuli. Black and red lines denote the disconnected and connected cases, respectively. C: PCA for population activities shown in B. By applying PCA to activity vectors whose elements correspond to activities of six LPTCs on the left and right hemispheres, we projected the activity vectors onto a two-dimensional space spanned by the first and second principal components, PC1 and PC2. Colors indicate different stimuli. In the disconnected case, four clusters of the activity vectors corresponding to the four different stimuli are respectively separated into the four quadrants, whereas in the connected case, clusters of the activity vectors corresponding to the in-phase and out-of-phase stimuli are respectively distributed along the PC1 and PC2 axes. D: Contribution ratio of PC1 and PC2 (bars) and cumulative contribution ratio (dots) in the connected and disconnected cases. (Mean $\pm$ s.e.m., 10 trials).

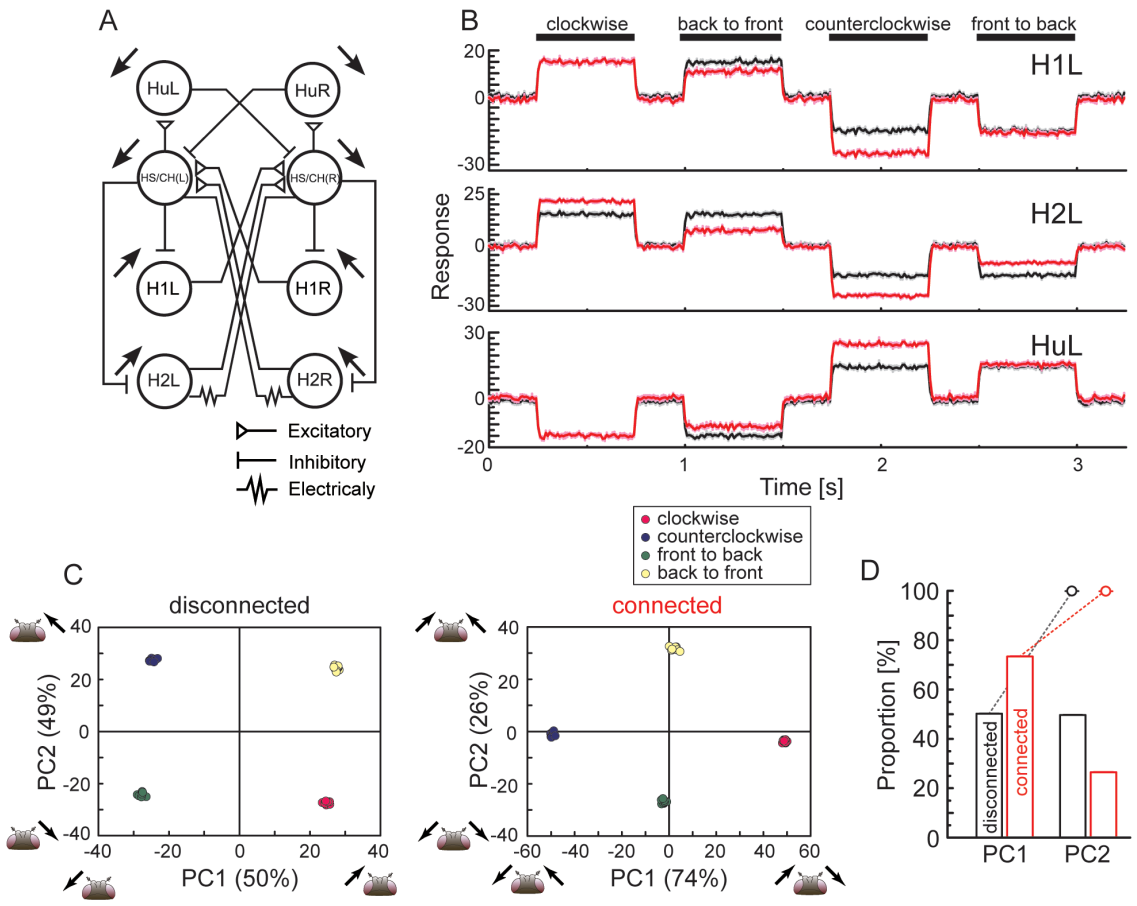
A
HuL
HuR
HS/CH(L)
HS/CH(R)
H1L
H1R
H2L
H2R
Excitatory
Inhibitory
Electricaly
B
clockwise
back to front
counterclockwise
front to back
H1L
H2L
HuL
Response
Time [s]
clockwise
counterclockwise
front to back
back to front
C
disconnected
connected
PC2 (49%)
PC1 (50%)
PC2 (26%)
PC1 (74%)
D
Proportion [%]
disconnected
connected
PC1
PC2

Figure 16 Each element of the first two principal components, PC1 and PC2, in five trials of numerical simulations for the reduced model with different random seeds for noise.

The upper table is the disconnected case, and the lower table is the connected case. What each principle component codes in the five trials is presented on the margins of these tables. In the connected case, PC1 and PC2 stably represent the in-phase and out-phase motions, whereas in the disconnected case, PC1 and PC2 are randomly assigned to either left or right monocular motion.

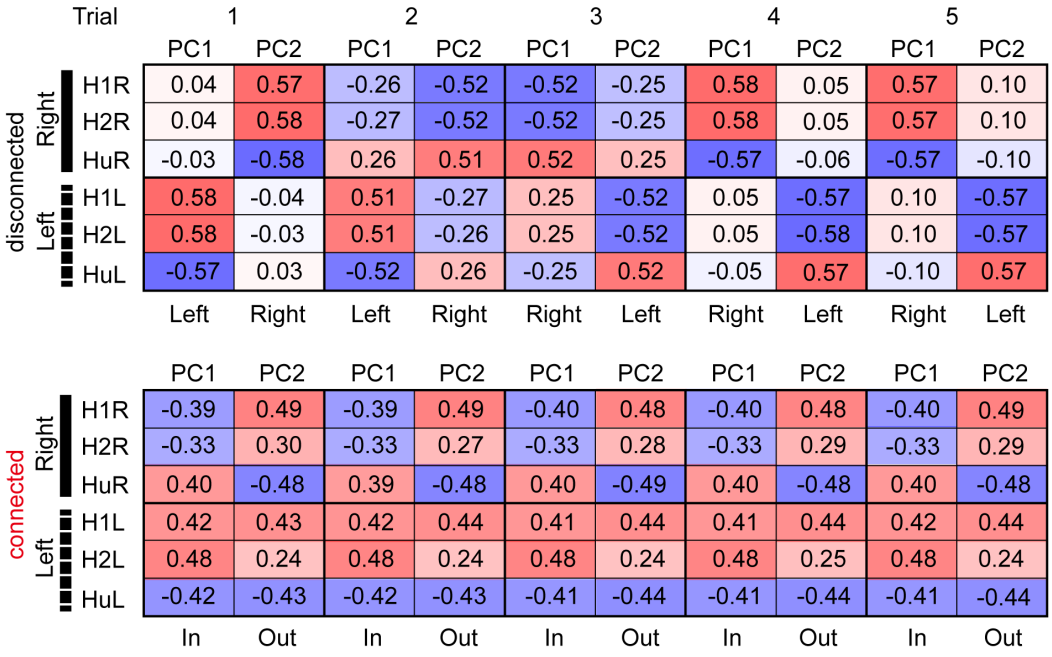
Trial
1
2
3
4
5
PC1
PC2
disconnected
Right
Left
H1R
H2R
HuR
H1L
H2L
HuL
0.04 0.57 -0.26 -0.52 -0.52 -0.25 0.58 0.05 0.57 0.10
0.04 0.58 -0.27 -0.52 -0.52 -0.25 0.58 0.05 0.57 0.10
-0.03 -0.58 0.26 0.51 0.52 0.25 -0.57 -0.06 -0.57 -0.10
0.58 -0.04 0.51 -0.27 0.25 -0.52 0.05 -0.57 0.10 -0.57
0.58 -0.03 0.51 -0.26 0.25 -0.52 0.05 -0.58 0.10 -0.57
-0.57 0.03 -0.52 0.26 -0.25 0.52 -0.05 0.57 -0.10 0.57
Left Right Left Right Right Left Right Left Right Left
connected
-0.39 0.49 -0.39 0.49 -0.40 0.48 -0.40 0.48 -0.40 0.49
-0.33 0.30 -0.33 0.27 -0.33 0.28 -0.33 0.29 -0.33 0.29
0.40 -0.48 0.39 -0.48 0.40 -0.49 0.40 -0.48 0.40 -0.48
0.42 0.43 0.42 0.44 0.41 0.44 0.41 0.44 0.42 0.44
0.48 0.24 0.48 0.24 0.48 0.24 0.48 0.25 0.48 0.24
-0.42 -0.43 -0.42 -0.43 -0.41 -0.44 -0.41 -0.44 -0.41 -0.44
In Out In Out In Out In Out In Out

Figure 17 Mechanisms of binocular integration of visual information.

Red and blue circles indicate depolarized and hyperpolarized cells in response to ipsilateral PD and ND motion stimuli, respectively. A: In the in-phase case, the cells responding to ipsilateral PD stimuli receive excitatory inputs from contralateral and ipsilateral LPTCs, and the cells responding to ipsilateral ND stimuli receive inhibitory inputs from the other LPTCs. The cells integrate the in-phase motion stimuli through their cooperative behavior. B, C: In the out-of-phase case, some cells responding to ipsilateral PD stimuli receive inhibitory inputs from the other LPTCs, and some cells responding to ipsilateral ND stimuli receive excitatory inputs from the other LPTCs. Thus, there is a frustration in the out-of-phase case because the activities of the neurons interfere with the mutual interactions.

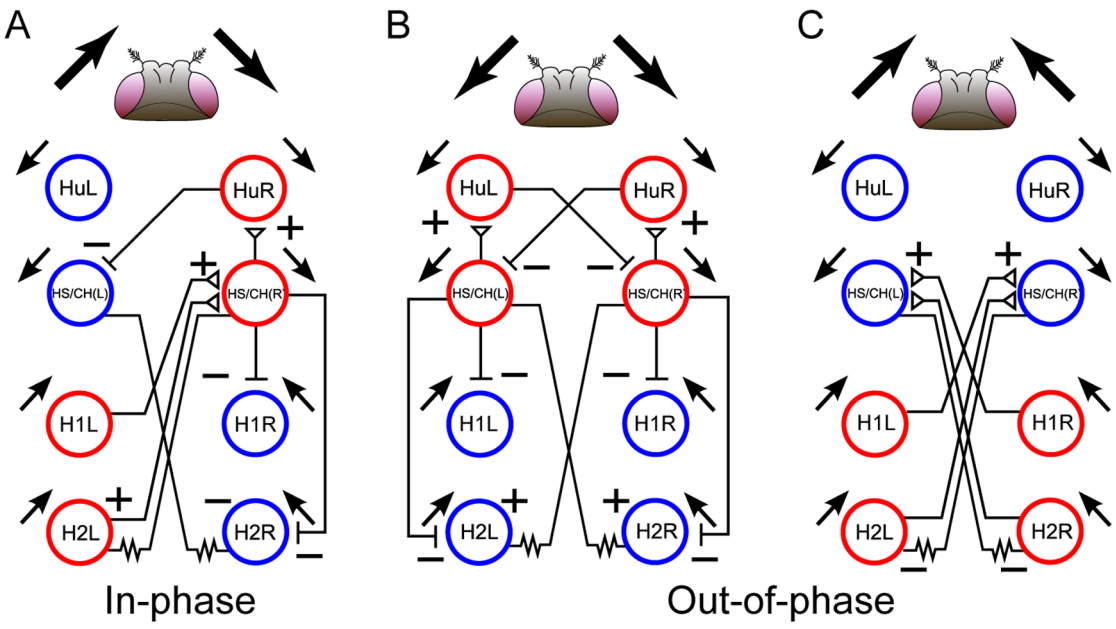
A
B
C
HuL
HuR
HS/CH(L)
HS/CH(R)
H1L
H1R
H2L
H2R
In-phase
Out-of-phase

Tables

Table 1 Morphological parameters and passive electrical parameters of each.

Cell type	Length μm	Diameter μm	$C_m\ \mu F/cm^2$	$E_{eq}\ mV$	$g_{leak}\ S/cm^2$
H1	1000	5	20		0.002
H2	200	5	20		0.002
Hu	200	5	20		0.002
HS	250	15	1	-50	0.001
CH	250	15	1	-50	0.001

Table 2 Parameters of the type-I Morris-Lecar model.

$V_{fast}\ mV$	$g_{fast}\ S/cm^2$	$V_{slow}\ mV$	$g_{slow}\ S/cm^2$	$V_{leak}\ mV$
120	0.004	-84	0.008	-60
$V_1\ mV$	$V_2\ mV$	$V_3\ mV$	$V_4\ mV$	$\phi/msec$
-1.2	18	12	17.4	0066

Table 3 Amplitude of the DC signal corresponding to PD and ND motion stimulus.

	H1	H2	HS
$S_p\ nA$	10	2	3.6
$S_N\ nA$	-1	-0.2	-1.3

Table 4 Combinations of either depolarizing or hyperpolarizing current for representing the four types of stimuli.

	C	CC	FB	BF
H1L	P	N	N	P
H2L	P	N	N	P
HuL	N	P	P	N
HSL	N	P	P	N
H1R	N	P	N	P
H2R	N	P	N	P
HuR	P	N	P	N
HSR	P	N	P	N